1500 years of lake sedimentation due to fire, earthquakes, floods and land clearance in the Oregon Coast Range: geomorphic sensitivity to floods during timber harvest period

K.N.D. Richardson,[1,†] J.A. Hatten[2*] and R.A. Wheatcroft[3]
[1] College of Earth, Ocean, and Atmospheric Sciences, Oregon State University, Corvallis, Oregon USA, 97331
[2] College of Forestry; Department of Forest Engineering, Resources and Management, Oregon State University, Corvallis, Oregon USA, 97331
[3] College of Earth, Ocean, and Atmospheric Sciences, Oregon State University, Corvallis, Oregon USA, 97331

*Correspondence to: J. A. Hatten, Oregon State University; College of Earth, Ocean, and Atmospheric Sciences; Corvallis, Oregon, USA, 97331. E-mail: jeff.hatten@oregonstate.edu
†Present address: United States Department of Agriculture Forest Service

ESPL

Earth Surface Processes and Landforms

ABSTRACT: Sediment cores retrieved from landslide-dammed Loon Lake recorded events back to the 5th century AD in a forested, mountainous catchment, thereby providing an opportunity to compare the impacts of known recent perturbations, including floods and timber harvesting with those of an early period in the cores, floods, fires, and earthquakes. High-resolution multi-parameter (grain size, %TC, %TN, and magnetic susceptibility) data allowed the core stratigraphy to be classified as background sedimentation and events. [137]Cs and radiocarbon dating, as well as a varved record in the last 75 years provided age control. Mean mass accumulation rate from 1939 to 1978 AD, the time of peak timber harvest and a cool wet phase of the Pacific Decadal Oscillation, was 0.79 (0.74–0.92, 95% C.L.) g cm^{-2} y^{-1}, significantly higher than mean rates of both the more recent contemporary period (coincident with the passing of the legislation that regulated harvesting practices in the region), 1979–2012 AD, at 0.58 (0.48-0.70) and the entire early period, 0.44 (0.41–0.46). Several event deposits are coeval with independently estimated ages of eight Cascadia subduction zone earthquakes in the early period, including the 1700 AD *Mw* 9.0 event. These deposits are predominantly formed by hyperpycnal flows, as are the known event deposits in the contemporary period. The high mass accumulation rate and greater frequency of thick event deposits during the early contemporary period point to the extraordinary role of timber harvesting in priming the landscape for subsequent sedimentary delivery during floods. Copyright © 2017 John Wiley & Sons, Ltd.

KEYWORDS: lake sedimentation; ^{137}Cs; earthquake; fire; timber harvesting; Oregon Coast Range

Introduction

Floods, earthquakes, and denudation of vegetation on the landscape by fire and anthropogenic land clearance (i.e. timber harvesting) act to mobilize and transport sediment from mountainous watersheds. Within mountains on tectonically active margins denudation rates can be high, where climate physically and chemically weathers regolith and bedrock (e.g. 0.05 to 0.3 mm y^{-1} in Oregon Coast Range; Reneau and Dietrich, 1990; Heimsath *et al.*, 2001). Therefore, lakes in these environments have the potential to capture an integrated record of processes affecting the sediment routing system and its response to human activities and other extreme events. Developing such a sedimentary record and being able to decipher its meaning contributes to an understanding of Earth system processes over a broad range of timescales, including the human timescale (Allen, 2008).

Research globally has shown that for years to decades following earthquakes, landslides may persist due to the weakening of the substrate and lowering the threshold for failure, thereby leading to elevated sediment fluxes from hillslopes (Crozier, 1986; Hovius *et al.*, 2011; Howarth *et al.*, 2012). Landslides and other erosional processes increase immediately post-fire and may persist for years (Swanson, 1981), and may account for a significant fraction (10–25%) of the long-term erosion in the Oregon Coast Range (Roering and Gerber, 2005; Jackson and Roering, 2009). Elevated erosion rates post-wildfire, and presumably post-earthquake, are controlled by hydroclimate (Warrick *et al.*, 2012). However, the long-term impact of this interaction of climate with fires and earthquakes on sediment dynamics is less well-known.

Forestry operations, such as road building, timber harvesting, and site preparation, can expose mineral soils, decrease infiltration capacities of soils, and increase erosion and peak flows

(Beschta, 1978; Jones and Grant, 1996; Swanson and Jones, 2002; Litschert and MacDonald, 2009; Hatten et al., 2018). After forest management activities on steep hillslopes, mass movements can result in substantial increases in suspended sediment transport to stream channels (Beschta, 1978). Historical practices conducted without riparian buffers or other protection measures increased the potential for delivery of sediment to streams (Beschta, 1978; Swanson and Jones, 2002). Timber harvest regulations and best management practices have been developed and implemented to reduce nonpoint source pollution associated with forest management activities (Ice, 2004). However, there have been many contradictory results from different studies of improved timber operations (Aust and Blinn, 2004; Anderson and Lockaby, 2011; Cristan et al., 2016). Therefore, there is a need to understand the impact of historical and contemporary practices on sediment dynamics in catchments dominated by intensive forest management.

The purpose of this research was to investigate changes in sedimentation in Loon Lake (LL), a small lake in the Oregon Coast Range whose catchment has been heavily impacted by timber harvesting and road building since the early 20th century. For several reasons, lakes can provide a high-fidelity record of events in a catchment. As an inland sink, lakes have accommodation space to trap a high proportion of inflowing particulates from the catchment (Owens and Slaymaker, 1993) and it is hydrodynamically unfavorable to remobilize material out of most lakes (Dearing, 1991; Wetzel, 2001). Additionally, anoxic bottom waters that are often present preclude bioturbation, thereby facilitating preservation of stratigraphy (Edmondson, 1991; Page et al., 1994, 2010). The relatively small source-to-sink area ratio of a lake allows for a rapid response to environmental changes and forcing variables (Cohen, 2003). Lastly, lake sediment accumulation rates can be rapid (0.1–4 cm y^{-1}), resulting in high-resolution records that are often seasonal to decadal (Cohen, 2003; Orpin et al., 2010).

By obtaining sediment records spanning the past ~1500 years from LL, we compared the relative contributions of sediment production and delivery by the four major perturbations within this catchment: earthquakes, forest fire, flood,

and timber harvesting. Herein we address the following questions and hypotheses: How are these forcings recorded in the lake sediment, i.e. what is the structure of the recorded beds, and what is their frequency? What role do large hydrologic events have in the sedimentation of the lake? We hypothesize that earthquakes would be recorded since this work is conducted within the Cascadia subduction zone (CSZ), but asked the question: how are they manifested? Also, how does sediment accumulation rate (SAR) change in response to events and background sedimentation through time? Lastly, can the effects of timber harvesting and changes in forestry practices after 1971 be detected within the sediment column? We hypothesize that timber harvesting would increase sediment accumulation rates, and that improvements in forest harvest practices would result in lower SAR. An annually-resolved record in the last 75 y allows a narrative of the interaction of hydrologic and anthropogenic forcings in the contemporary period, and a window into understanding past forcings, represented by the stratigraphy of the early period.

Methods

Study area

Loon Lake is a 4-km-long landslide-dammed lake located 30 km east of the Pacific Ocean within the Oregon Coast Range (OCR) (43.585° N, 123.839° W; Figure 1). With an elevation of 128 m, LL has a surface area of 1.2 km^2 and a catchment area of 230 km^2. It lies within the western hemlock (Tsuga heterophylla) vegetation zone (Franklin and Dyrness, 1988) and is underlain by the Eocene-aged Tyee and Elkton Formations (Baldwin, 1974), which contain rhythmic, thickly bedded sandstone and interbedded carbonaceous siltstone. Within these steep and deeply dissected mountains (total relief of 680 m), deep-seated landslides, shallow landslides, and debris flows dominate hillslope geomorphic processes and sediment transport out of unchanneled valleys on low-order tributaries (Dietrich and Dunne, 1978; Heimsath et al., 2001; Roering et al., 2005).
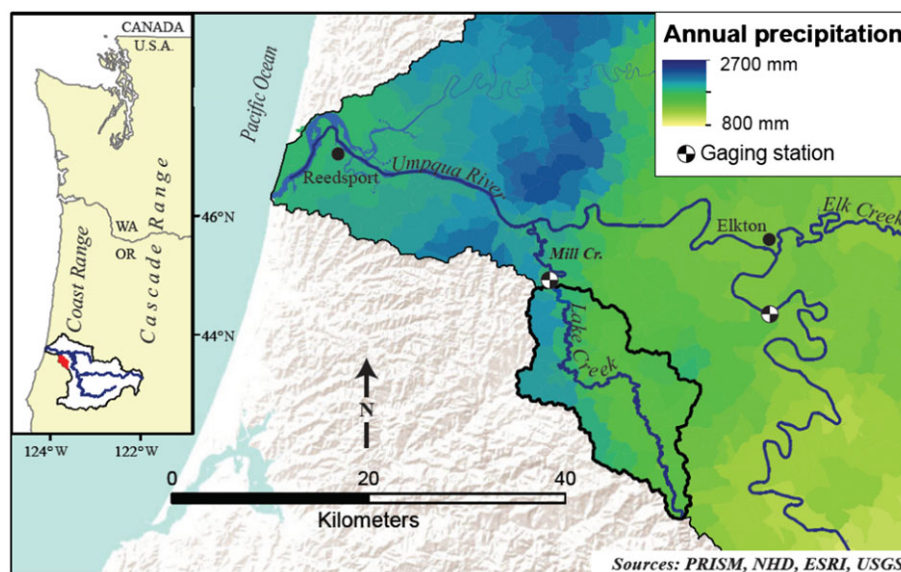

Figure 1. Lower Umpqua River Basin and precipitation. LL catchment is shown in red on the regional map of a portion of Cascadia (left), and outlined in black on the Umpqua basin and precipitation map. LL is at the north end of the catchment, south of the gaging station at Mill Creek (USGS #14323000). Elkton gaging station (USGS# 14321000) is ~20 km east of LL catchment. Sources: PRISM Climate Group (2004), National Hydrology Data set (NHD), Environmental Systems Research Institute (ESRI), 1998. [Colour figure can be viewed at wileyonlinelibrary.com]

In Cascadia, natural forcings such as extreme floods, megathrust earthquakes, and wildfires that may be recorded in sedimentary sinks are numerous. Average annual precipitation in the LL catchment is 1700–2400 mm (Figure 1), falling mostly as rain in November – April, with summertime drought. Occasionally, high intensity, long-duration rainfall events from so-called 'atmospheric rivers' (Ralph and Dettinger, 2012) punctuate the usual wintertime low-intensity precipitation and result in regional flooding. Recent extreme precipitation events in the area occurred in water years (WY) 1965, 1982, 1996, and 1997 (a summary of historical events can be found in the Supplementary materials section and Table S1). The Pacific Decadal Oscillation (PDO; Mantua et al., 1997) has been shown to influence inter-annual stream flow and the magnitude of peak flows in the Umpqua River basin (Wheatcroft et al., 2013), of which the LL catchment is a part.

Lying within the Cascadia subduction zone (CSZ), LL has experienced several earthquakes during its approximately 1.6 ky existence (Leonard et al., 2010; USGS, 2012). These megathrust earthquakes periodically shake the regolith (Nelson et al., 2006) at a recurrence interval of between 260 and 600 y, depending on along-margin location (Witter et al., 2012), and have estimated moment magnitudes of 8 to 9 (Goldfinger et al., 2012). While fire in the OCR prior to anthropogenic suppression recurred every 230 ± 30 y (Long et al., 2007). Landslides and other erosional processes increase immediately post-fire and persist for years (Swanson, 1981), and may account for a significant fraction (10–25%) of the long-term erosion in the OCR (Roering and Gerber, 2005; Jackson and Roering, 2009). Based on historical accounts and inferences from dendrochronology, the only large fires in the LL catchment occurred at about 1765 and 1868 AD. Given that the last large fire occurred in 1868 AD, and that the last CSZ earthquake occurred in 1700 AD (Table S1), the catchment has been free of these two perturbations for ~150 y.

Human actions, especially timber harvesting and associated activities such as road building have impacted the LL catchment for the past ~120 y. Although timber was harvested around LL early in the 20th century (USDI, 2005), it did not begin in earnest until the 1940s in the Elliott State Forest and BLM lands (Figure 1; USDI, 2005) as well as in the upper catchment. During the 1950s the lake was used as a log dump (USDI, 2005). In the 1960s, timber harvest sharply increased by the largest landowner, a private company (Figures 2(a), S1), so that by 1971 about 20% of the catchment had been harvested. From 1972 to 2012, ~50% more of the LL catchment was harvested (Figure 2(c)), reaching peak harvest in the 1970s. During the period of peak logging, the 1971 Oregon Forest Practices Act was passed (Oregon, 2001). As a result, rules on timber harvest best management practices began to be implemented (Hairston-Strang et al., 2008). Recent work has shown that contemporary harvesting practices in western Oregon have little impact on suspended sediment concentrations and fluxes (Hatten et al., 2018). We hypothesize that the passing of the Oregon Forest Practices Act would be associated with a reduction in sedimentation in LL, however the magnitude of any change is uncertain.

Physicochemical properties of LL itself play important roles in its sedimentation. The lake has an average and maximum depth of 16 and 32 m, respectively, and flows out over the sandstone landslide-debris dam as Mill Creek (Figure 2(a)–(d)). It develops a strong thermocline in the summer and becomes isothermal in the winter (Curtiss et al., 1984). During and following high-magnitude rainfalls, the lake level was observed to rise and water became turbid for days to months. Beyond episodic storm turbidity, water quality has changed in the 20th century. While the lake was used as a log dump, the water was said to be brown

(Phillips, pers. com., 2015). The likely effect of rapid extinction of light at shallow depths may have inhibited photosynthesis by phytoplankton (Schuytema and Shankland, 1976). Additionally, bacterial decomposition of organic matter in the water column may have increased dissolved oxygen demand (Ho and Ching-Yan, 1987), possibly leading to anoxic conditions in the lake bottom. In November 1977, the USGS measured dissolved oxygen profiles and found the water at the bottom of the lake to be anoxic (Rinella, 1979). In the 1980s it was noted that algae populations in the water column increased in the summer and that bottom water dissolved oxygen was again depleted (Curtiss et al., 1984). Finally, the lake was shown to be somewhat productive (mesotrophic) in the 1990s (Oregon DEQ, 1992).

Coring

Three sampling expeditions in 2013 yielded 20 cores of which three were chosen for detailed analysis in this study (Table I). Information on the other cores collected in this project can be found in Richardson (2017). A Nesje corer (Nesje, 1992) and a custom-built pontoon boat were used to recover the two longest cores (02aN and 02bN), which were taken in the deepest basin approximately 5 m apart. These act as replicate cores, and most of the sediment analyses were done with these and a large-diameter gravity core also from the deep basin (02 N, Figure 2(b)). The Nesje cores were cut on the pontoon boat into ~1.5 m sections, but at slightly different lengths to preserve all stratigraphy. Cores were placed in an upright position until split, and were refrigerated at 3°C at the field site and while in storage at the OSU Marine and Geology Repository (OSU-MGR).

Sediment core analyses

Whole cores were scanned by X-ray computed tomography (CT) at OSU's Veterinary Hospital within 8 d of coring, producing X-radiographs that allow visual inspection and measurement of core stratigraphy and assessment of relative density based on gray scale value. They were then run through a Multi-Sensor Core Logger (MSCL) for measurement of wet bulk density by gamma-ray attenuation. Dry bulk density (g cm^{-3}) was calculated by standard techniques from wet bulk density (Dadey et al., 1992), and then was used to calculate dry sediment mass. Using mass instead of length in sedimentation rate calculations allows comparison of rates throughout the core by accounting for in situ compaction of sediment (Besonen et al., 2008), as was observed in Loon Lake cores.

Cores were split and described according to standard techniques within weeks to months of collection. For grain size and elemental analysis, bulk sediment samples were removed in 1-cm increments the entire length of core 02aN, and in some sections in cores 02bN and 02 N after the cores were stratigraphically correlated. A roughly 6 g sub-sample from each depth interval was heated to 70°C in a hot water bath and treated to one to several treatments of hydrogen peroxide (30% H_2O_2) to remove organic material so that only the mineralogic fraction remained for grain size analysis (Gray et al., 2010). Grain size was then measured on a Malvern Mastersizer 2000 following methods described in Sperazza et al. (2004). The output is grain size in 100 bins as a percentage of the total volume of sample.

For elemental analysis, 10–20 mg aliquots were combusted at high-temperature in a Flash EA1112 Elemental Analyzer that yielded weight-percent total carbon (%TC) and total nitrogen
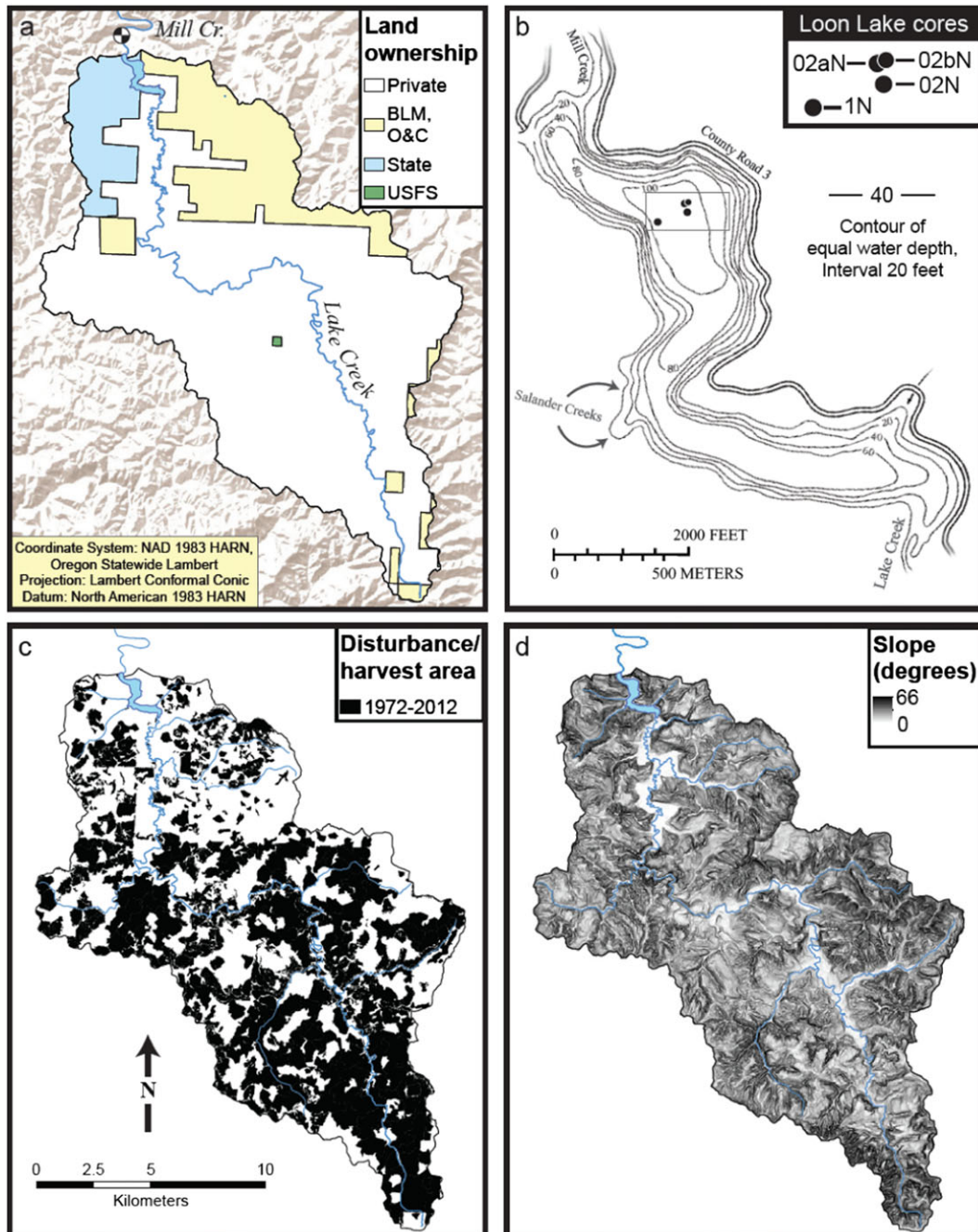
Figure 2. LL catchment: land ownership, lake bathymetry, harvest, slope. (A) Land ownership and Mill Creek gaging station location. (B) LL bathymetry and core locations of key cores (map adapted from Rinella, 1979 and Curtiss *et al.*, 1984). C) Harvest area 1972–2012 AD detected by remote sensing (Cohen *et al.*, 2002; Kennedy *et al.*, 2012). D) Slope of terrain; flat valley south and above lake (shown as white) is probably the old lake bed. [Colour figure can be viewed at wileyonlinelibrary.com]

Table I. Metadata for cores used in this study. Coring devices used were Nesje percussion piston corer (PC) and large-diameter gravity corer (GC)

Core name	Date taken	Inner core diameter (cm)	Original length (m)	Latitude (°N)	Longitude (°W)	Depth of water (m)	Coring device
02aN	9/12/2013	7.3	7.03	43.59166	123.83901	31	PC
02bN	9/12/2013	7.3	6.26	43.59165	123.83907	31	PC
02 N	9/13/2013	10.1	1.67	43.59139	123.83894	31	GC

(%TN). In a separate analysis, 30 representative samples throughout the core were vapor acidified to determine the percentage inorganic C (Hedges and Stern, 1984). This analysis showed that <5% of samples have inorganic C, likely from bedrock. Because of the possibility of inorganic carbon (IC) being present, albeit small, the %TC will continue to be referred to as such, while recognizing the predominance of organic carbon.

Core chronology and mass accumulation rates

To date the recent past, ^{137}Cs and ^{210}Pb activities were measured by γ-ray spectroscopy (Wheatcroft and Sommerfield, 2005). Samples were taken from core 02 N in 0.5- and 1-cm-thick increments, freeze-dried, ground with a mortar and pestle, and stored in polystyrene counting jars. Samples were counted for >24 h on two Canberra Low Energy Germanium (LEGe) detectors and the 46.5, 352 and 661.6 keV photopeaks used to quantify activities of ^{210}Pb, ^{214}Pb (to estimated supported levels of ^{210}Pb) and ^{137}Cs, respectively (Wheatcroft and Sommerfield, 2005). Activities of ^{210}Pb and ^{214}Pb were consistently near or below detection limits and so were not considered further. Once the depths of the 1963 peak of atmospheric ^{137}Cs deposition and 1953 date of onset were identified, these locations were correlated with the smaller diameter Nesje cores, 02aN and 02bN, using the CT scans.

Linear and dry mass accumulation rates (SAR, MAR; cm y^{-1}, g cm^{-2} y^{-1}) in the recent past (hereafter, 'contemporary period') were calculated as both a simple ratio of sediment mass accumulated by time as well as a by the slope of a regression line of accumulated sediment over time. To address how mass accumulation rates have changed in response to various forcings in the contemporary period, two different periods about a single breakpoint were compared. To test for significance of difference in the two periods' MARs, a multiple regression separate lines model with a climate covariate from correlated instrumental data was used (Ramsey and Schafer, 2013). The covariate in the model was discharge (Q) from the nearby gaging station on the Umpqua River at Elkton (Figure 1) because there is a strong correlation between this gage and the gagge at Mill Creek, outflow of LL (Figures 2(a), S4). The regression model to compare contemporary period MAR was accomplished by generalized least squares with R statistical software (R Development Core Team, 2016), and accounted for lack of independence and homogeneity in the residuals (Table S2; Zuur et al., 2009). When comparing MAR between the contemporary periods and earlier periods, mean MAR was estimated without the Q covariate in the regression model because of the absence of instrumental data in the earlier periods.

The breakpoint was determined by considering the period of recovery following timber harvest. In studies of timber harvesting practices employed prior to the Oregon Forest Practice Act of 1971, road building, harvesting, and site-preparation resulted in elevated suspended sediment for 2–10 y in paired watershed studies in this region (Swanson and Jones, 2002; Beschta and Jackson, 2008; Keppeler, 2012). In a watershed most comparable to LL (same physiographic region and geologic formation) suspended sediment yields returned to pre-harvest fluxes after 7 y in the Alsea Watershed Study (1959–1973; Beschta and Jackson, 2008; Hatten et al., 2018. Therefore, many roads and harvest units within the LL watershed are likely to produce elevated suspended sediment for several years after harvesting rules were passed. To account for this lag we implemented a 7-y lag in our analysis (breakpoint at 1978-1979).

To obtain macrofossils for radiocarbon dating of the 'early period' (i.e. pre-1880), 1-cm-thick core slices were wet-sieved in search of minimally degraded material of sufficient mass (~1 mg) that typically consisted of leaves, needles, and cone-bracts. After physical cleaning, samples were chemically treated with an acid-alkali-acid wash (Björck and Wohlfarth, 2001), dried, and sent to the National Ocean Sciences Accelerator Mass Spectrometry (NOSAMS) Laboratory for analysis. The resulting ^{14}C dates were calibrated with Oxcal program v4.2.4 (Bronk Ramsey, 2009a) with the IntCal13 atmospheric curve data set (Reimer et al., 2013). The output was likelihood probability distributions expressed in 2∂ ranges. By applying prior knowledge about possible non-steady sediment deposition (Bronk Ramsey, 2008) and outliers (Bronk Ramsey, 2009b), Oxcal generated marginal posterior densities (MPDs), and with those, calculated calibrated age ranges referred to as highest posterior densities (hpd; Figures S6, S7).

Sediment and mass accumulation rates were calculated with the marginal posterior densities (MPDs). Using a Monte Carlo (MC) approach, by resampling with replacement (n=5000) from these distributions, a representative sample of rates was developed using R statistical software (R Development Core Team, 2016; Blaauw, 2010; Richardson, 2017). Summary statistics on the sampling distribution could then describe an estimated sediment and mass accumulation rate. The MPDs were used for this purpose instead of median or other single central value because the single point does not accurately represent the range of years in which the calibrated year could actually be (Telford et al., 2004) and the densities are generally multimodal (e.g. ^{14}C sample LL2; Figures S6, S7). Specifically, a single age within each of the MPDs was drawn, weighted by its probability of ages within the distribution. With the draws from the ages and their associated depths, a least squares regression was constructed, and from this a MAR and SAR was calculated. Resampling in this manner continued until 5000 stratigraphically-correct draws were obtained and the resulting estimated rates were accrued. To examine changes in MAR in shorter lengths of time in the past, the same method of MC type resampling from the MPDs was used to build distributions of MAR of core regions bound by ^{14}C dated layers.

Between the early ^{14}C-dated period and the contemporary ^{137}Cs-dated period exists a 'gap period', where there is no direct chronology. To estimate the MARs in this interval, summary statistics were calculated from a distribution as was done for the ^{14}C-calibrated dates. MC type method resampled between the MPD of the most recent ^{14}C calibrated age (excluding outliers) and the age of the bottom layer of the contemporary period.

Results

Core stratigraphy

X-radiographs of cores 02aN and 02bN reveal a rich stratigraphy that is comprised of distinct layers, beds up to 23 cm thick, and sections of quasi-homogeneous fabric (Figure 3). Based on the CT, grain size, and elemental data in cores 02aN and 02bN, seven stratigraphic units are identified: distinct layers, indistinct layered sections, mottled units, graded beds, coarse homogeneous layers, clay drapes, and a unique fine sand bed topped with weakly graded silt (Figure 4).

Viewed in the X-radiographs, distinct layers are comprised of couplets that alternate between lighter layers (more X-ray opaque), indicating denser material, and generally thinner, less dense dark layers (Figures 3, 4(a) and Table II). Where distinct layers are preserved throughout the core, their mass distributions are remarkably similar, except for a section in the upper part of the core at 26–67 cm where more massive layers exist (Figure 5). It is also within this section, including the layers above, i.e., the top 67 cm of the core, the upper and lower contacts of layers are sharper than the rest of the core. When light and dark layers are separated, the dark layers are found to be carbon- and nitrogen-rich (medians of 3.11% and 0.30%, respectively; Figure S3) and the light layers, which are thicker and bias the average of the
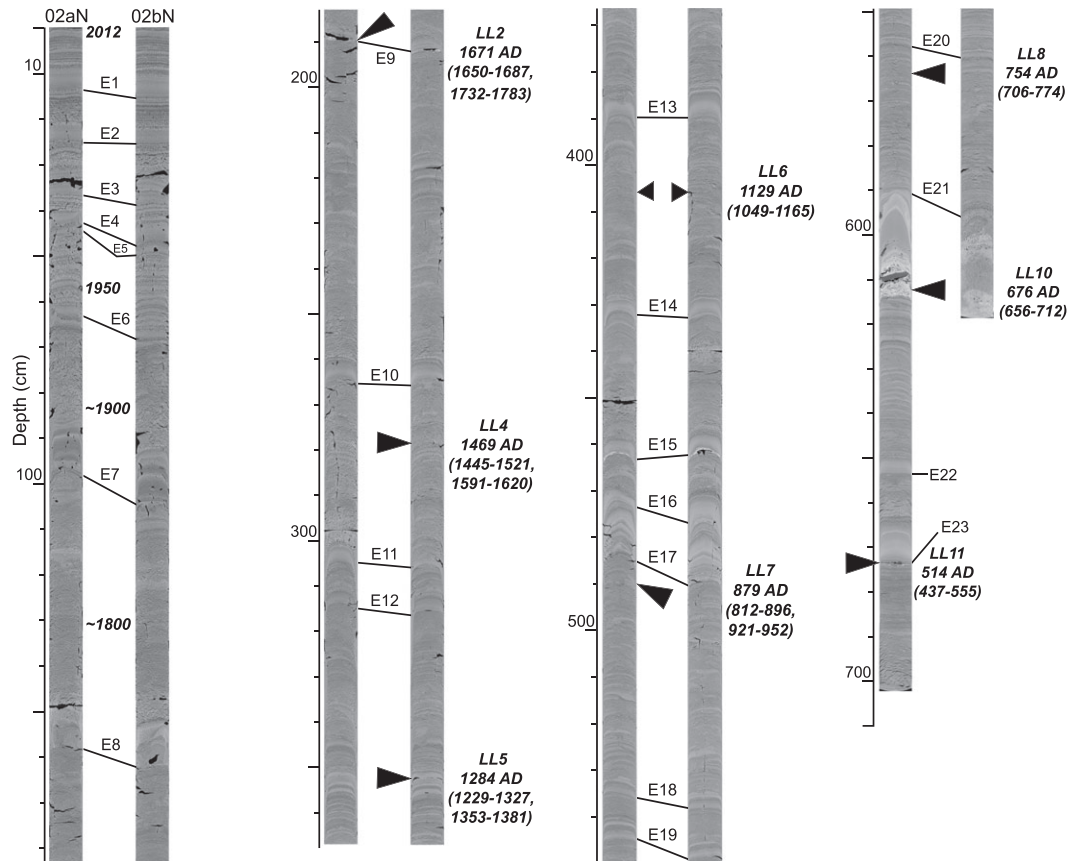
Figure 3. Stratigraphic correlation of Cores 02aN and 02bN. Depth is marked in centimeters from the X-radiographs. Event beds (e.g. E1) are labeled at their bases, except E21, and are stratigraphically correlated between the two cores. The cores are broken into four sections, from top to bottom, l to r. Locations of ^{14}C sample extraction are indicated by the point of a bold triangle on the core(s) from which the material came. Above each sample point are the calibrated median ages of ^{14}C-dated material used in the age–depth model, labeled with their sample name (e.g. LL2), along with their 95% highest posterior density ranges (hpd). On the top part of the core (~0–170 cm), 2012 AD marks the first full water year varve near the sediment–water interface (SWI). 1950 AD is found by varve counting. ~1900 and ~1800 AD are approximate ages based on application of mass accumulation rates. Core 02bN ends above the bottom of event bed E21, so this event is stratigraphically correlated at the top of the event bed.

distinctly layered intervals, are less so (medians of 2.04% and 0.16%, respectively). Distinct layers comprise 16% of the mass of the sediment column of core 02aN.

Indistinct layered and mottled units have similar grain size and geochemistry to distinct layers (Table III). Layers exist in the indistinct layered sections, but are rare and difficult to quantify in their lateral extent and thickness (Figure 4(b)). In mottled sections, clasts and specks with similar grey scale values to light layers are surrounded by a homogeneous matrix, and appear to be broken pieces of layers (Figure 4(c)). Distributed within and between the distinctly layered sections, indistinct layered and mottled sections dominate the core, occupying 68% of its mass. Because these layers have similar grain size and geochemical parameters (Figure 6, Table III), we suggest that the indistinct layered and mottled sections are distinct layers in various stages of alteration due to post-depositional reworking. Therefore, these three units are combined into one association and will be referred to as 'background sedimentation'.

Throughout the core there are layers that punctuate the background stratigraphy. Twenty-three were identified throughout the core, ranging in thickness from 1.1–23.9 cm and consisting of graded beds with clay drapes of at least 34% clay. They have been correlated, numbered, and labeled (e.g. E1, E2; Figure 3, Table IV). Although most of these layers contain two or three subunits: a basal homogeneous layer (Figure 4f), a graded bed (Figure 4(d)–(f) and part of Figure 4(a)), and a clay drape (Figure 4(f)), the deposits manifest themselves in different ways. Their internal structure suggests more rapid deposition than the

surrounding background sedimentation, and therefore are referred to as an association of 'event beds' hereafter. Several event beds have a thin, coarse layer, bright in the X-radiograph, with a sharp basal contact with the background stratigraphy (e.g. Figure 4(f)) that often contains allochthonous material such as relatively coarse (~1 mm) fragments of leaves, twigs, and charred and non-charred wood fragments. Even if this coarse layer, referred to as the basal homogeneous layer, is not present, nearly all of the event beds have a sharp basal contact. The main body of the event beds is a graded bed, which in the CT scans shows as a gradation in density, most often from dark to light to dark (e.g. Figure 4 (e)). These grey scale variations are reflected in the grain size and the elemental data. In the grain size data, above the base there is usually thin inverse grading, and then thicker normal grading, first briefly coarsening from clayey silt to silt or sandy silt and then fining upward to the clayey silt or silty clay drape (Figures 4(e)–(f); Table III).

Although the 23 event beds are remarkably similar in their grading sequence, there are a few exceptions. Beds E7 and E8 have unusual features – E7 has the largest sustained %TC anomaly of the entire 02aN core (Figure S2), and both have a 4–6 cm massive fine sand-rich layer within. The thickest event bed of the core, E21 (Figure 4(d)), has a thick fine sandy base 8.9 cm, thick and opaque in the x-radiograph, with a sharp, possibly erosional contact with the background sediment below. Although this sandy base is analyzed as a separate unit because of unique characteristics (Tables II and III; Figures 3 and 4(d)) such as coarse woody debris, it is integrally part of
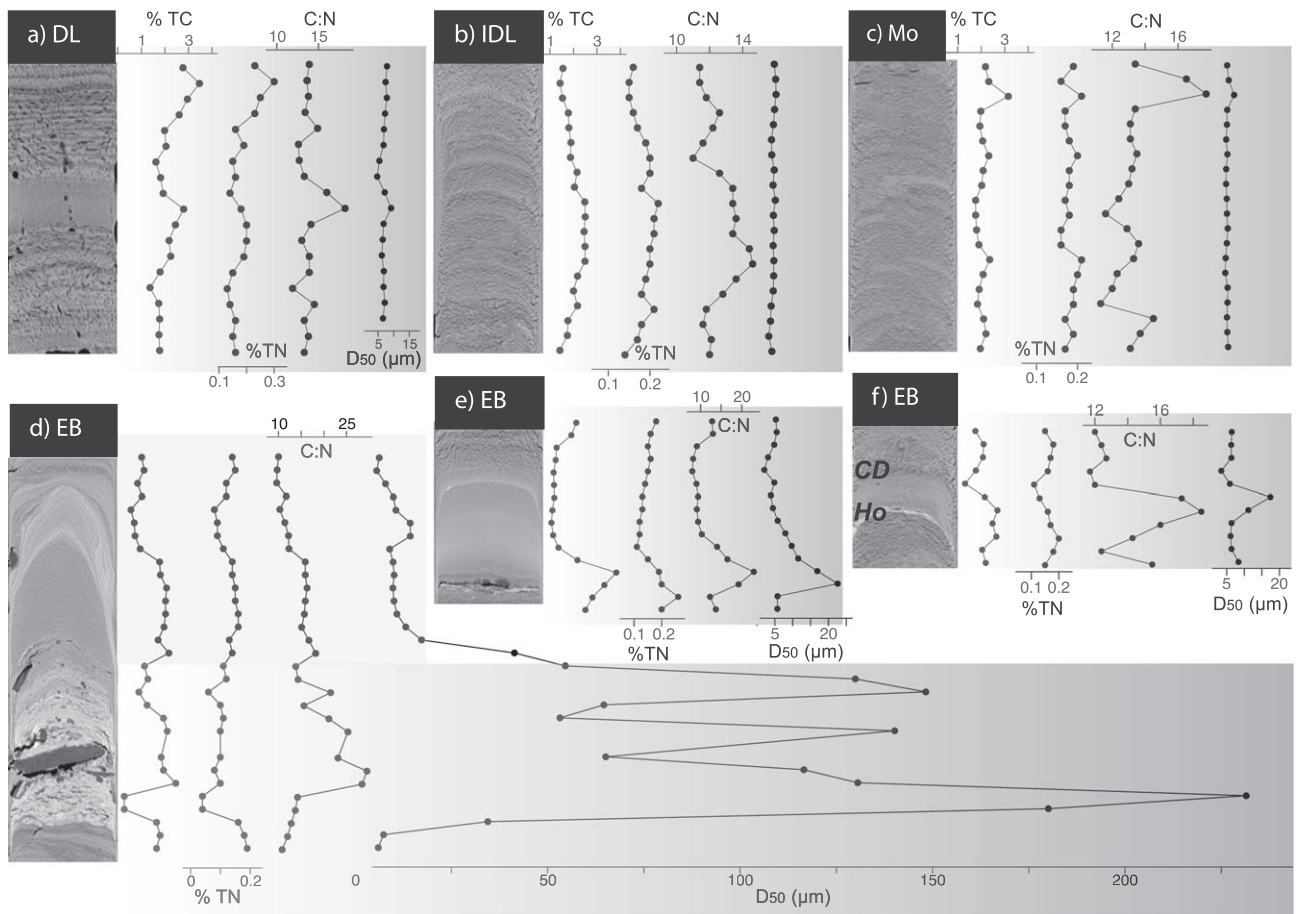
Figure 4. Seven stratigraphic units displayed by X-radiographs and parameter plots. The units in the top row (l to r) are distinct layers (DL), indistinct layered sections (IDL), and mottled sections (Mo). On the bottom row are three examples of event beds (EB): (d) sand and woody debris event bed E21; (e) graded bed; and (f) graded bed with clay drape (CD) as gradual upper contact and homogeneous layer (Ho) at sharp basal contact. Parameters for each core piece are (l to r): %TC (total carbon), %TN (total nitrogen), C:N (atomic), and median grain size (D_{50}). Scales are different for most parameters, so most have their own ordinate axis. Scale for %TC is common vertically for a-d, b-e, c-f, respectively, and also in D_{50} for b-e and c-f. The D_{50} parameter for EB(d) fills more than half of the bottom of the figure. Core pieces are from the following CT depths in core 02aN: a) 14–33 cm; (b) 367–386 cm; (c) 489–508 cm; (d) 588–616 cm; (e) 663–675 cm; (f) 457–467 cm.

bed E21, as it transitions to a weakly graded silt layer, for a total thickness of 23 cm.

Despite the variations within the graded beds, their grain size distributions and geochemical characteristics are differentiated from the background sedimentation (Tables II and III, Figures 6 and 7). When viewed over the entire core, the measured characteristics for background sedimentation are relatively uniform with depth, but are more variable for the event beds, which are clearly outside the range of the background sedimentation (Figure 7).

The distinguishing characteristics of event beds are that %clay is lower, the mean D_{50} is an order of magnitude larger, the %TN is lower, and C:N reaches 18 on the 75th percentile of the boxplot (Figure 6), compared with 13 for the background sediment. As expected, for all parameters, the interquartile range is much wider for graded beds (Figure 6) than for other stratigraphic units. Homogeneous layers are similar in most of their characteristics with graded beds, but are so thin that their measurements of parameters included sediment from both the background sediment and graded bed above. Clay drapes range in thickness from 0.13 cm to 1.34 cm. They have the highest mean clay content of all stratigraphic units, the lowest mean D_{50}, and the lowest mean C/N.

The event bed association constitutes 16% of the mass of the core. There are several other layers in the core which could potentially be event deposits, but did not meet the criteria of having a clay drape and their thicknesses were similar to

normal winter deposition in the contemporary period. Some appear graded, and some may possibly be graded but the resolution of sampling could not detect this. For consistency throughout the analysis, these layers were not included in the event bed association. As with the 23 event beds previously identified, these are distributed fairly uniformly throughout the core, except for the upper 67 cm of the core, where event beds and thicker light layers are more frequent (Table IV). Therefore, there will be a consistent error where background MAR is slightly biased high.

Core chronology and mass accumulation rates: contemporary period

Once the stratum of the 1963 AD ^{137}Cs fallout peak had been identified (Figure 8(d)–(f)), it became evident that the light–dark couplets present in the top 67 cm of the core were annually deposited, and are therefore varves (Edmondson, 1991; Dean and Bradbury, 1993). The top part of the two Nesje cores and the gravity core show consistency in their layer sequencing with 50 couplets, so it appears that the 2013 sediment–water interface was preserved. Two thick event beds near the core top are coincident with large regional floods in WYs 1982 and 1997, and additionally, another thick layer follows two layers above the 1963 layer,

Table II. Description and thickness of stratigraphic units. Descriptions are in terms of both the actual core sediment and of the X-radiograph (Sed, CT, respectively). Layers are broken into components to show the difference in thicknesses and parts. The sand layer is a single unique unit at the bottom of a graded layer at 6 m depth, thus only one thickness value is given. Units are combined into two associations based on origin

| Unit association	Stratigraphic unit name	Unit descriptions		Thickness (cm)		
				Mean	**Median**	**Range**
Background sedimentation						
	Distinct layers	*Sed:* Alternating thick olive gray and thin dark brown/black layers; *CT:* Alternating thick light (more dense) and dark (less dense) layers; gassy fabric; *Sed below 70 cm:* "light" layers are dark, as in graded beds	*Light*	0.41	0.31	0.04-2.15
			Dark	0.25	0.19	0.06-0.62
	Indistinct layered units	*Sed:* Brown homogenous mud matrix intercalated with few and faint thin dark or thick light layers; *CT:* Dark matrix with few and faint complete thicker light and thinner dark layers; gassy fabric		2.78	2.3	0.59-10.11
	Mottled units	*Sed:* Brown homogenous mud matrix with lighter-value mottles; *CT:* Dark matrix mottled with amorphous chunks of lighter (denser) sediment; gassy fabric		3.47	1.24	0.59-17.07
Event layers						
	Clay drape	*Sed:* Light brown layer generally with gradual contact from graded layer below to next layer above; *CT:* Darker layer atop graded layer; gassy		0.5	0.44	0.13-1.34
	Graded	*Sed:* Usually normal grading, with dark brown at base grading to light brown clay drape; *CT:* Grading upward from dark to light; variations include lighter (denser) area in middle and darker near top and/or alternating thin light and dark layers with sharp contacts at top (pulses); not gassy		4.89	3.02	1.15-23.88
	Homogeneous	*Sed:* Generally, thin dark brown layer with sharp lower contact at the base of graded beds; *CT:* Thin, bright white layer with sharp lower contact; contains much allochthonous debris; not gassy		0.47	0.47	0.12-0.90
	Sand layer	*Sed:* Dark brown layer with sharp basal contact, grading upward to clayey silt; unconsolidated; *CT:* Bright white thick layer with sharp basal contact; contains woody debris and voids		One layer; thickness = 8.89 cm		
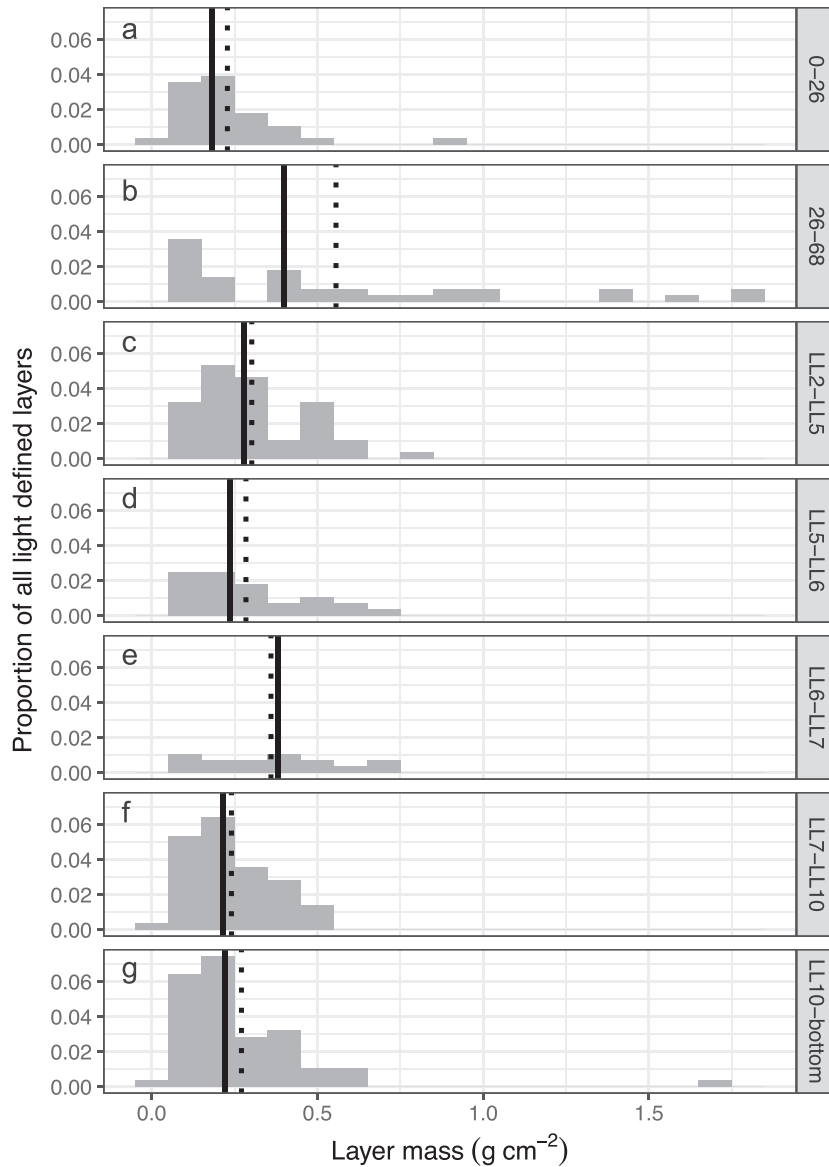
Figure 5. Distributions of light layer mass through the sedimentary column. These are represented by proportional histograms for sections through the core. Sections are delineated by location in the core which captures groups of layers, and are conveniently bounded by the ^{14}C sample intervals. The sections of the core which have the highest concentrations of distinct layers are 0–26 cm, 26–67 cm, LL5–LL6, LL7–LL10, and LL10–end. See Figure 3 for the locations on the CT scans of these intervals. The whole core is represented, except 68–190 cm (LL2) where there are only two preserved distinct layers. The vertical solid black line is the median of each distribution, and the dotted black line is the mean.

which is coincident with a large regional flood during WY 1965, as shown at the nearby gaging station on the Umpqua River at Elkton (Figure 1; Figure S5). Layers were counted downward in the core from 1963 until 1939 ($\pm$ 2 y), at which point the sediment becomes mottled. Varve chronologies often have extra or missing layers (Zolitschka *et al.*, 2015 and references therein). By comparing layers across LL cores we minimized varve counting error. We are confident in the ages of thick event beds above 1963 and layers in between due to the consistency in ^{137}Cs marker and observation of large floods at the lake during regional storm events. Below this marker bed to 1939, we applied a $\pm$ 2 y counting error for the gap and early period MAR analysis. The boundary at 1939 divides the contemporary period from the gap and early periods of the core.

Once the varves had been identified, a MAR for the top 65.6 cm (51.4 g cm^{-2}) of the core was found to be 0.69 g cm^{-2} y[-1] by calculating a simple ratio (Table V). The MAR for before and after the 1978 breakpoint of 1978 is 0.79 and 0.58 g cm^{-2} y[-1], respectively. These can be expressed as SARs of 1 and 0.75 cm y[-1], and an overall SAR of 0.89 cm y[-1].

Using the regression model with the Q covariate, the result of the test of difference in rates between before and after 1978 shows that there is strong evidence that the estimated mean difference in MAR of 0.24 (0.07–0.42) g cm^{-2} y[-1] is different from 0 ($F_{1,69}=7.26$, $P=0.0088$; Table S2). The estimated early contemporary period mean MAR of 0.83 (0.74–0.92) g cm^{-2} y[-1] is greater than that of the late contemporary period MAR of 0.59 (0.48–0.70) g cm^{-2} y[-1] (Figure 9 inset, Table S2).

By removing the event-bed layers, an event-bed-free stratigraphic column of accumulating mass with depth – 'event-free depth' or 'EFD' (Bronk Ramsey *et al.*, 2012) is established, and reflects the background sediment accumulation rate (Brown *et al.*, 2002; Page and Trustrum, 2010; Howarth *et al.*, 2013). In this way, an age-mass model is constructed in the contemporary period that allows interpretation of age with mass unbiased by thick event beds (Figure 9). As

Table III. Stratigraphic unit summary statistics of grain size and geochemistry. Each row includes the mean (standard deviation) of six grain size parameters and three geochemical parameters, and the descriptive name for the majority and secondary clastic class of samples in the unit. The far-left column groups units into two associations based on origin

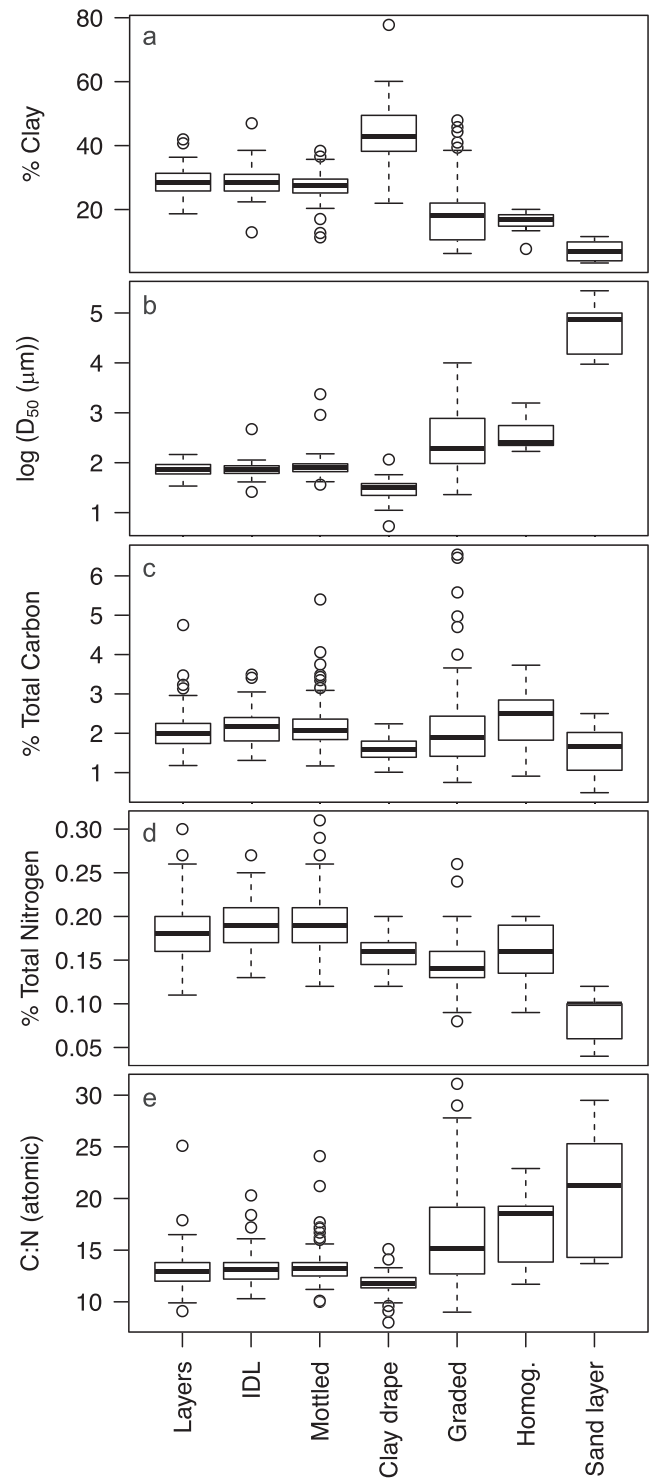| Unit association	Stratigraphic unit name	D_{10} (μm)	D_{50} (μm)	D_{90} (μm)	% clay	% silt	% sand	C:N (atomic)	% TC	% TN	Textural classification[1]
Background sedimentation	Distinct layers	2.08 (0.22)	6.51 (0.81)	22.71 (11.31)	28.43 (4.17)	69.01 (4.80)	2.55 (1.69)	12.92 (1.69)	2.04 (0.48)	0.18 (0.03)	Clayey silt, silt
	Indistinct layered units	2.05 (0.20)	6.51 (1.00)	22.18 (4.14)	28.79 (4.01)	68.71 (4.44)	2.51 (1.47)	13.16 (1.40)	2.15 (0.42)	0.19 (0.03)	Clayey silt, silt
	Mottled units	2.12 (0.18)	6.83 (1.70)	23.20 (7.82)	27.38 (3.38)	70.04 (3.35)	2.58 (2.41)	13.28 (1.37)	2.15 (0.47)	0.19 (0.03)	Clayey silt, silt
Event layers	Clay drape	1.49 (0.60)	4.49 (1.16)	15.85 (4.09)	44.16 (11.13)	54.68 (10.85)	1.16 (1.36)	11.74 (1.53)	1.59 (0.31)	0.16 (0.02)	Clayey silt, silty clay
	Graded	3.10 (0.95)	13.56 (9.83)	41.40 (29.95)	18.57 (9.66)	74.90 (9.52)	6.52 (9.00)	16.22 (4.92)	2.16 (1.15)	0.15 (0.03)	Silt grading to clayey silt, or to silty clay, at times with sandy silt base
	Homogeneous	3.01 (0.83)	13.86 (5.37)	71.76 (25.84)	15.87 (4.18)	70.78 (4.39)	13.60 (6.40)	17.04 (4.09)	2.36 (1.00)	0.16 (0.04)	Clayey silt, sandy silt
	Sand layer	7.86 (4.78)	125.98 (55.42)	454.59 (85.15)	6.84 (2.90)	28.7 (8.28)	64.46 (11.06)	20.67 (5.99)	1.55 (0.70)	0.08 (0.03)	Silty sand, sand

Figure 6. Variation of grain size and geochemical parameters. Boxplots display variation, median, and outliers of grain size and geochemical parameters by the seven major depositional units in the core: distinct layers, indistinct layered sections (IDL), mottled units, clay drape, graded beds, homogeneous layers, and the sand-woody debris bed (E21). Parameters shown are % clay by volume, log of median grain size (D_{50}), weight % total carbon and nitrogen, and carbon to nitrogen atomic ratio. D_{50} is shown in log scale for visual clarity.

in all-depths (Figure 9 inset), there is also strong evidence that the estimated mean difference in background (EFD) MAR of 0.28 (0.12–0.44) g cm^{-2} y^{-1} is different from 0 ($F_{1,63}$=11.28, *P*=0.0013; Table S2), and that the early EFD MAR is greater than that of the late contemporary period EFD MAR (Table V).

Table IV. List of 23 event beds. These were defined by a minimum %clay in the drape over the preserved graded bed. These beds were removed to calculate a background sedimentation rate (EFD). Estimated year is derived by varve counting for event beds 1–6, and an estimation by applying the resulting background sedimentation rate of 0.38 g cm^{-2} y^{-1} for event beds 9–23, and a background sedimentation rate of 0.54 g cm^{-2} y^{-1} for the 'gap' period in between (event beds 7 and 8), then rounded to the nearest 10 y. Prediction intervals are shown graphically in Richardson (2017; Figure A10). Event bed depth measured according to the Multi-Sensor Core Logger (MSCL) is the scale for sampling and parameter measurements. Thickness and calculated mass measurements are derived from the X-radiographs ('depth CT'). Possible forcing includes those factors other than climate, storms, and floods that could have contributed to the event and include TH: timber harvest, LC: land clearing, F: fire, EQ: earthquake. Each listing of possible force is labeled if there is evidence of occurrence

Event bed number	Estimated water year (AD)	Event depth MSCL (cm)	Event depth CT (cm)	% clay cap	Layer thickness (cm)	Dry mass (g cm^{-2})	Possible forcing
1	1997	11	14	46.7	4.7	5.1	**TH, LC**
2	1982	22	24.8	37.6	3.9	4.2	**TH, LC**
3	1971	33	36.8	43.1	2.3	2.3	**TH, LC**
4	1965	39	43.4	35.3	2.3	2.8	**TH, LC**
5	1964	41	45.5	50.8	1.7	1.4	**TH, LC**
6	1946	59	63.3	39.8	2.0	2.3	**TH, LC**
7	1890	91	96.8	34.4	9.6	7.7	**F, LC**
8	1770	152	157.8	37.5	10.9	10.6	**F**
9	1690	185	190.0	44.1	3.4	3.1	**EQ**
10	1470	259	265.7	56.0	4.8	5.5	**EQ**
11	1370	298	304.7	42.7	3.7	4.3	**EQ**
12	1350	308	313.9	41.5	2.2	2.3	EQ
13	1150	383	389.4	38.9	3.0	3.8	**EQ**
14	1030	425	431.6	41.2	2.7	3.0	
15	940	456	462.3	53.7	2.7	2.2	EQ
16	920	466	472.8	44.8	2.9	2.2	EQ
17	920	478	484.5	48.2	10.2	9.2	**EQ**
18	760	528	534.9	43.2	1.2	0.9	EQ
19	740	538	544.6	60.1	1.6	1.2	EQ
20	710	552	557.2	39.7	1.5	1.1	EQ
21	630	610	613.7	22.0	23.9	30.3	**EQ**
22	550	646	653.4	53.0	3.2	2.8	EQ
23	510	667	673.5	77.8	8.1	9.8	**EQ**

Core chronology and mass accumulation rates: early period

Terrestrial macrofossils throughout the core provided 11 dates (Table VI). Eight were used, and three were identified as outliers and were not used in further analysis. Analyzing the likelihood distributions with a deposition model and an upper boundary constraint at 1939 AD ± 2 y in Oxcal resulted in modeled posterior densities (MPDs) and age–mass and age–depth models (Figures 10, S6, respectively). Monte Carlo resampling of the eight distributions resulted in an estimated mean MAR and a 95% confidence interval (CI) with the 2.5% and 97.5% quantiles of the MC distribution. The estimated mean MAR (CI) for the entire ^{14}C period is 0.44 (0.41–0.46) g cm^{-2} y^{-1}. The estimated mean MAR between shorter core regions in the early period are all similar to this MAR except for a faster MAR between dated layers of LL7 and LL10 (Table V). The result for EFD MAR for the overall early period is 0.38 (0.34–0.40) g cm^{-2} y^{-1}. With this MAR, a final age-mass model for the ^{14}C period was constructed with prediction intervals for age unbiased by instantaneous deposition (Figure A10 in Richardson, 2017). Estimated event bed ages were calculated with this model (Table IV).

Core chronology and mass accumulation rates: gap period

MC type method resampled the marginal posterior density distribution of the LL2 sample (bimodal peaks of 1651–1688,1733–1784 AD) and 1937–41 AD (1939 ± 2 y). The result is an estimated mean MAR for the gap of 0.62 (0.53–0.96) g cm^{-2} y^{-1}, and an estimated mean EFD MAR of 0.54 (0.47–0.85) g cm^{-2} y^{-1} (Table V).

Discussion

Origin and preservation of the units

Examination of the distinctly layered couplets formed during the contemporary period suggests they are varves. Dark layers have higher %TN and %TC and lower C/N ratios than light layers, strongly indicating algal productivity (cf. Edmondson, 1991). The lighter and generally thicker layers have lower %TN and %TC, and slightly higher C/N, suggesting increased allochthonous input. Fluvial input of sediment to OCR lakes is minimal during the summer, whereas normal winter precipitation delivers allochthonous materials to the lake by more voluminous and energetic flows. These turbulent flows support coarser grain sizes, and although grain size was not measured on the light and dark layers separately, the light layers in the X-radiograph indicate denser, minerogenic material. Therefore, the couplet formation in the contemporary period is summer dark layers alternating with lighter winter layers of normal annual low- to moderate-discharge floods.

It is reasonable to assume that the process of varve formation has remained essentially the same over time within the sediment column, given that the climate of the Pacific Northwest has not markedly changed during the past two millennia (Minckley and Whitlock, 2000). However, in the early period of the core there are few distinct varves, rather the stratigraphy is dominated by mottled or indistinct layered units suggestive of post-depositional reworking, such as bioturbation or gas migration. A specific mechanism for the preservation of the varves in
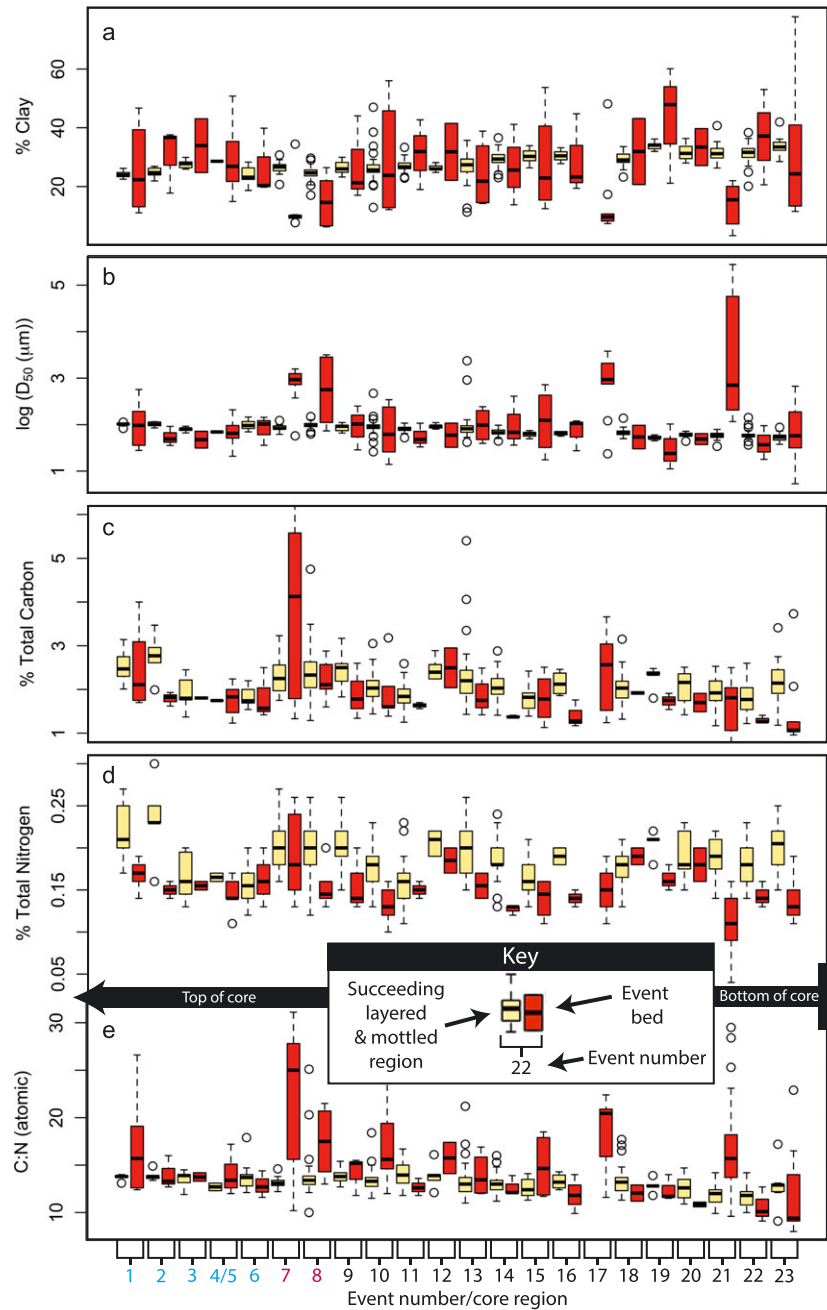
Figure 7. Select parameters of event beds and background sediment. Parameters included are % clay, D_{50}, %TC, %TN, C:N. Each pair consists of an event bed boxplot on the right (red) and a boxplot for the succeeding background sedimentation on the left (yellow), up to the next event. All 23 event beds in the core are represented, although E4 and E5 are adjacent in the core, so were combined in this figure. Distributions consist only of values from samples whose sediment comprised approximately 100% of the two associations (events and background sedimentation). Because of small sample sizes, in three cases no values were available to report within regions/event beds 17–19, and in several cases for event beds, only one sample result was available to report (event beds 3, 6, 12, and 20), which shows as a flat bar in the figure. The bottom of event bed distribution E21 is cut off for visual clarity; it has 0.5% TC. E1–6 (blue font) represent industrial timber harvest era. E7 and E8 (red font) are during time of known wildfire. [Colour figure can be viewed at wileyonlinelibrary.com]

the contemporary period is the eutrophication of the lake, starting when logs were rafted on the lake at the beginning of major timber harvest in the catchment. Others have noted preserved varves and layers following eutrophication (Karlin and Abella, 1992; Page *et al.*, 1994).

Scattered throughout the core there are units formed by events that are better preserved due to higher mass and thickness compared to other deposits. The preservation of event beds increases as SAR increases, as the thickness of the bed increases, and as bioturbation intensity and depth decrease (Wheatcroft, 1990). The smooth fabric and lack of gas bubbles visible in the CT scans indicate that bioturbation was not as extensive in the thick event beds.

The grain size sequence within most of the contemporary period event beds consists of a thin zone of inverse then normal grading, which is interpreted to reflect the waxing and waning of flows associated with high-magnitude floods (Mulder and Alexander, 2001). The resulting deposit is termed a 'hyperpycnites' (Hofmann and Hendrix, 2010), and its structure can vary due to flood hydrograph differences, sediment flux, and distance from inlet. Hyperpycnal flows support suspension of larger grains to the deep basin, often traveling great distances through a lake. This would account for the coarse homogeneous layer at the base of several of the event beds. Since the lake is not thermally stratified during flooding in the winter but rather is mixed, it is expected that
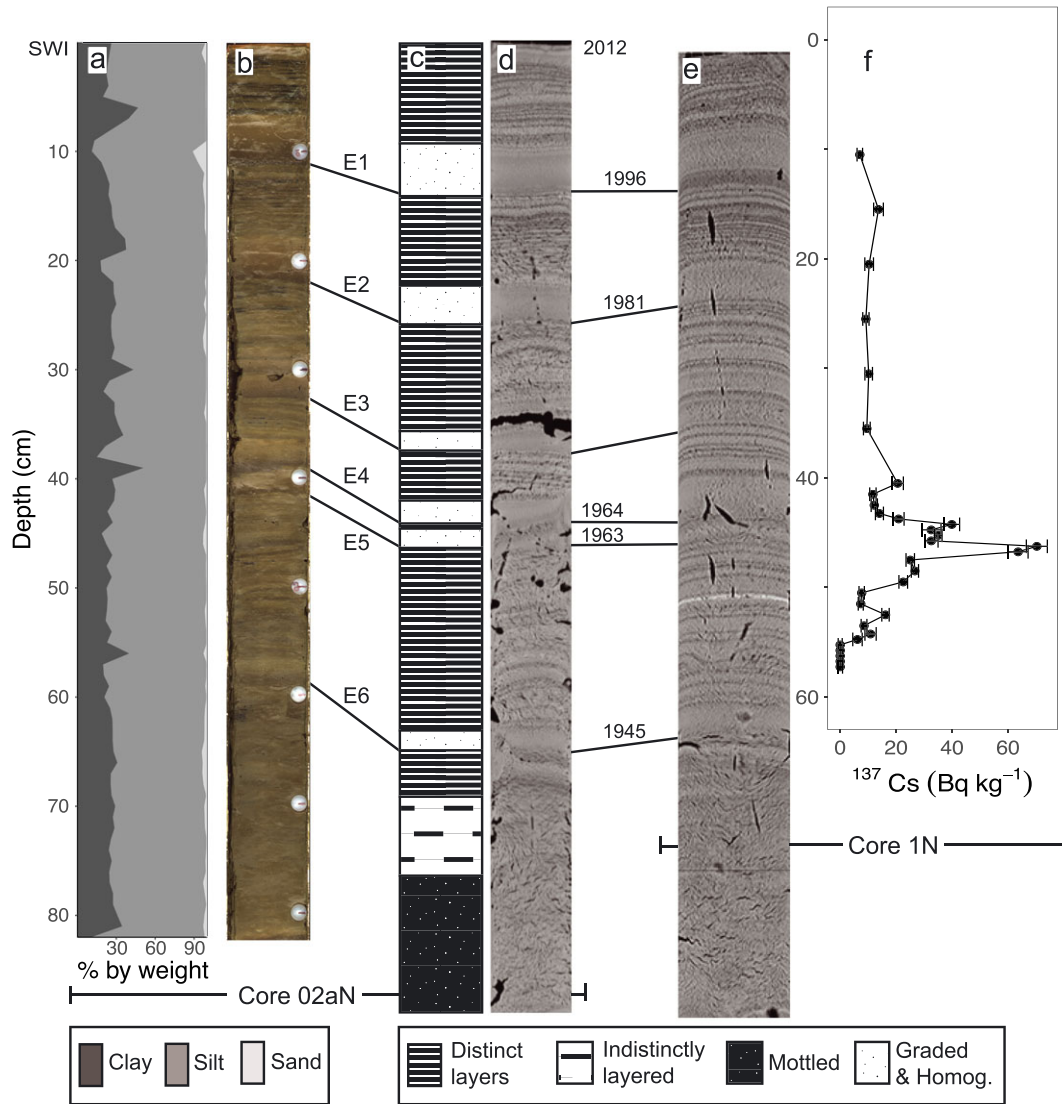
Figure 8. ^{137}Cs profile of Core 1 N and stratigraphic units of Core 02aN. Upper 82 cm of Core 02aN (a-d) and stratigraphic equivalent of Core 1 N (e-f), showing: (a) vertical stacked area plot of %clay, silt, and sand, respectively, measured at 1-cm increments (legend below plot); (b) color photo; (c) cartoon representation of the five stratigraphic units (legend below plot); and (d) X-radiograph of the center slice of the core. The stacked area plot is stratigraphically paired with the photograph and the cartoon is stratigraphically paired with the CT scan, demonstrating the disparity in length between the two pairs. This can be explained by the dewatering and consolidation of the sediment that occurred between the time of coring and immediate CT scanning, and delayed splitting, photographing, and destructive measurements of this core. Core 1 N is shown on the right by (e) X-radiograph and (f) ^{137}Cs profile of this core. Event beds 1–6 are labeled and their stratigraphic position on both cores are indicated by lines at the base of the bed. The ^{137}Cs 1963 AD peak can be traced across the cores immediately below E5. SWI = sediment water interface. [Colour figure can be viewed at wileyonlinelibrary.com]

fine particles would remain in the water column for some time. It has been observed that for days and months following floods the LL water is still turbid and the particles continue to settle out of suspension. This is the condition by which the clay drape is deposited, composed of the finest sediment. Hyperpycnites, and therefore these event layers, are supported by large sediment fluxes which might be more common after disturbances such as fire, earthquakes, land clearance, and timber harvesting.

The grain size and geochemical signatures of the contemporary event beds also support an allochthonous origin with high-energy delivery, and are outside the range of background sedimentation. The contrast between background sedimentation and event beds is consistent with the trend that with higher discharge, grain size and C/N increase as found in the Coast Range Alsea River north of LL (Hatten *et al.*, 2012). The range of values presented, varied between low flows with fine grain size (C/N = 10–16), and higher flows (C/N 14–25), parallel the contrast between LL background sedimentation

(C/N 12–14) and graded beds (C/N 13–19) (Figure 7). Further, as the event bed grain size fines upward, the %TC and C/N decreased. The clay cap atop the graded bed was below background sedimentation levels of C/N, which is consistent with erosion of deep soil horizons with low %TC and C/N.

Additional geochemical evidence of the LL event beds being of an allochthonous source is the spike in %TC and especially C/N at the bottom of the bed. This is an expected result because of an increase in coarse organic matter, which is high in non-degraded (i.e. recently fixed) carbon indicated by elevated %OC and C/N, being delivered at the beginning of flood events from the catchment. This is consistent with other lake research: the initial increase in %OC at the onset at the base of the bed in a lake in Spain (Moreno *et al.*, 2008), and high C/N at the base of turbidites attributed to fluvial delivery in Lake Paringa, New Zealand (Howarth *et al.*, 2012). Other lake studies also show an agreement with the geochemical description of event beds described here (Brown *et al.*, 2002). Sub-aqueous landslides from the steep walls of the lake or from resuspension of lake-

Table V. Mass and sediment (linear) accumulation rates. Rates for the contemporary periods are calculated by simple ratios of depth to time for mass accumulation and for sediment (linear) accumulation ('sed/time') and by least squares regression without the climate covariate for trans-period comparison ('regression'). Rates for ^{14}C period are mean estimated slopes calculated by regression after resampling of highest probability densities of eight dated samples, LL2-LL11. Confidence intervals of the Monte Carlo (MC) type sampling are 5th and 95th quantiles of the distribution. 'EFD' is event-free depth, where events have been removed and a mean estimated background accumulation rate is calculated. 'All depths' have all layers present in the calculation

| Period (cal y AD)	Dry mass accumulation rate (g cm^{-2} y^{-1})				Sediment accumulation rate (cm y^{-1})		Method	Events
	All depths		EFD		All depths	EFD		
	mean	95% C.I.	mean	95% C.I.				
contemporary								
2012-1979	0.59	(0.48-0.70)	0.28	(0.24-0.33)			regression	1,2
	0.58		0.31		0.75	0.47	sed/time	
1978-1939	0.83	(0.74-0.92)	0.56	(0.38-0.74)			regression	3-6
	0.79		0.57		1.00	0.75	sed/time	
2012-1939	0.70	(0.59-0.82)	0.44	(0.34-0.54)			regression	1-6
	0.69		0.45		0.89	0.63	sed/time	
"gap"								
1939-1671	0.62	(0.53-0.96)	0.54	(0.47-0.85)			MC (1939-LL2)	7,8
early period - overall								
1671-514	0.44	(0.41-0.46)	0.38	(0.34-0.40)	0.40 (0.38-0.42)	0.35 (0.34-0.36)	MC (LL2-LL11)	9-23
early period - core regions								
1671-1284	0.46	(0.36-0.59)	0.42	(0.33-0.54)			MC (LL2-LL5)	9-12
1284-1129	0.35	(0.21-0.58)	0.33	(0.20-0.54)			MC (LL5-LL6)	13
1129-879	0.40	(0.28-0.64)	0.33	(0.23-0.53)			MC (LL6-LL7)	14-17
879-676	0.69	(0.46-1.07)	0.54	(0.37-0.82)			MC (LL7-LL10)	18-21
676-514	0.36	(0.24-0.51)	0.27	(0.17-0.38)			MC (LL10-LL11)	22,23
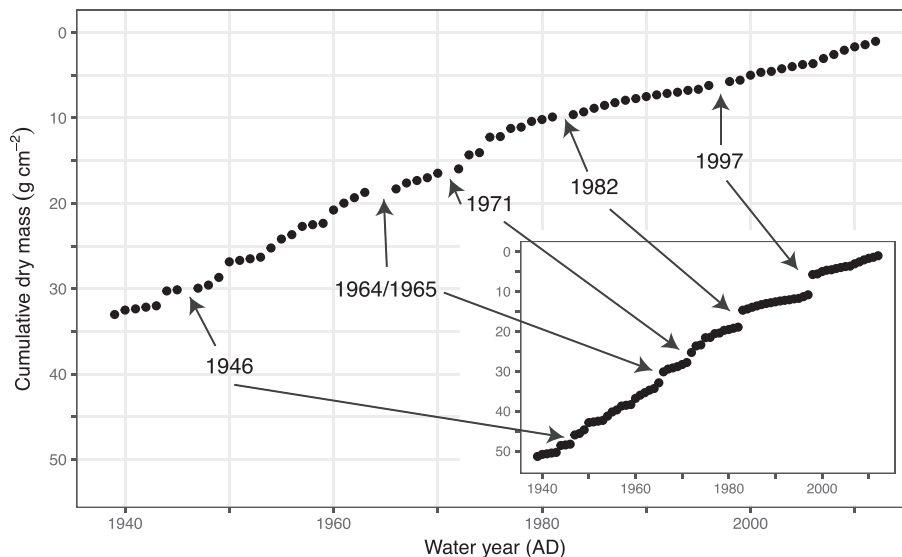
Figure 9. Age–mass model of the contemporary period of Core 02aN. Depth is represented on the y-axis by cumulative dry mass down the core with event beds E1–6 removed (EFD). Within the inset graph, the y-axis is also cumulative dry mass, but with all depths represented. The six most massive beds in the contemporary period are labeled by the years in which they occurred, and with an arrow pointing to the missing value, or in the case of the inset graph, to the occurrences of relatively instantaneously deposited sediment, represented by a gap. For both EFD, and all-depths (inset), the climate covariate is included in the model and the difference in estimated mean mass accumulation rates between the periods 1939–1978 and 1979–2012 is significant, with a difference (confidence interval) of 0.28 (0.12–0.44) g cm^{-2} y^{-1} and 0.24 (0.07–0.42) g cm^{-2} y^{-1}, EDF and all-depths respectively (Table S2).

bottom sediments (Karlin *et al.*, 2004; Orpin *et al.*, 2010) are not likely the mechanism of event bed deposition at LL in the contemporary period, because the event beds on average have different characteristics from the background sedimentation (Figure 7 and Tables II and III).

All of the event beds earlier than E7 except E14, occur within the estimated age range of a Cascadia subduction zone (CSZ) earthquake (Table VII), so it is possible that some of these beds were deposited either co- or post-seismically. In Lake Paringa, for example, deposits indicating hyperpycnal turbidity currents were recorded on top of co-seismic deposits of reworked lacustrine sediment, indicating delivery by catchment landsliding and post-seismic sediment-laden fluvial discharge after direct co-seismic deposits of reworked sediment (Howarth *et al.*, 2012). In a survey of lakes in the Pacific Northwest, Morey *et al.* (2013) also found synchroneity between the offshore earthquake record and lake deposits. At LL, most of the deposits have the characteristics of delivery by hyperpycnal flow, not by direct co-seismic deposition, so would have been a result of increased sediment supply within the fluvial system, regardless of the mechanism for production of sediment. One exception was E21, which has very high sand content that probably could not have been supported by a hyperpycnal flow and therefore delivered directly to the lake. LiDAR derived DEM show evidence of a landslide that occurred on LL's surface on the west side, possibly co-seismically to support this assertion. However, for most of the post-seismic events, earthquakes produce sediment delivered to the lake as a post-seismic contribution, but neither the exact mass accumulation rate can be distinguished from that produced by other perturbations (Howarth *et al.*, 2012), nor can the length of time sediment is contributed by this source be defined (Hovius *et al.*, 2011), partly because of lack of sufficient age control early in the core.

Event beds 7 and 8 in particular were likely created by high rainfall events acting on hillslopes destabilized by fire and transported to the depositional center within the lake by hyperconcentrated density flows (Mulder and Alexander, 2001). Like timber harvest, fire leaves the thick soil mantle susceptible to landsliding, and plays an important role in the

delivery of sediment to fluvial systems in the OCR. After event bed E9, during 1765 and 1868 AD, there are two known fires of large spatial extent in the catchment that are temporally near E7 and E8.

Mass accumulation rates

To address how mass accumulation rates have changed in response to various forcings, different time periods were compared. First, two periods within the contemporary period were compared: 1939–1978 AD (early contemporary) when the PDO was wet and cool and when timber harvest was at its peak, and 1979–2012 AD (late contemporary) when improved forest harvest practices were assumed to be in place, harvest rates were lower, and the climate was drier (Figures S1, S5). Second, the early and late contemporary periods were compared with both the radiocarbon-dated period (early period) of the core, and the gap period (Table V).

The significant result of the test of difference in rates in the contemporary period between before and after 1978 (Table V and S2) suggests that the sediment accumulation rate was associated with a change in forcings such as hydroclimate and/or harvesting. The choice of 1978 as our breakpoint was justified by many studies examining suspended sediments in regional paired watershed studies. To examine this choice we ran the same statistical analysis with 1972 as the breakpoint (the year after the Oregon Forest Practice Act was passed). With this stricter breakpoint, the trends were the same as the 1978 analysis, but the statistical tests fell outside our chosen alpha (a=0.05). While the analyses that included all depths and the event-free data-set resulted in no significant difference between before and after 1972 (*P*= 0.064 and 0.057, respectively), the confidence intervals generated using this stricter break point do not change any of the conclusions when comparing the contemporary periods with the gap and pre-settlement periods of the core.

The early contemporary period MAR of 0.83 (0.74–0.92) g cm^{-2} y^{-1} was entirely within the range of the gap period (0.62 (0.53–0.96) g cm^{-2} y^{-1}), and is almost twice the rate of the early

Table VI. Samples submitted for radiocarbon dates. Bolded sample names are those samples used in age–depth model. Date ranges are the 95.4% (2∂) likelihood probability distribution ranges (unmodeled) and highest posterior density ranges (hpd; modeled). Depth is in MSCL scale. NSF Cooperative Agreement number, OCE-0753487

| Sample name	Accession #	¹⁴C Age (BP)	Depth correlated in 02aN (cm)	Source core	Material	Unmodeled calibrated date range (2∂ BC/AD)	Modeled calibrated date range (2∂ cal. AD)	Median calibrated date (cal. AD)
LL1	OS-113277	270 +/- 20	152-153	02 N	Coniferous/deciduous leaf	1522-1572, 1630-1666, 1784-1795	--	--
LL2	OS-113278	190 +/- 20	183-184	02aN	Coniferous/deciduous leaf; twig	1661-1684, 1735-1806, 1931-1951	1651-1688, 1733-1784	1671
LL3	OS-113279	430 +/- 20	227-229	02aN, 02bN	Coniferous/deciduous leaf	1430-1479	--	--
LL4	OS-113280	385 +/- 20	271	02bN	Deciduous leaf	1445-1521, 1591-1620	1445-1515	1469
LL5	OS-113392	685 +/- 50	346	02bN	Broadleaf (or deciduous) leaf	1252-1400	1229-1327, 1353-1381	1284
LL6	OS-113281	915 +/- 20	398-401	02aN, 02bN	Coniferous/deciduous leaf; cone bract	1036-1165	1049-1165	1129
LL7	OS-113282	1190 +/- 20	484	02aN	Coniferous/deciduous leaf	773-888	812-896, 921-952	879
LL8	OS-113283	1280 +/- 20	558	02aN	Deciduous leaf	672-770	706-774	754
LL9	OS-113284	2830 +/- 25	599	02aN	Coniferous/deciduous leaf; some charred	1051-914 BC		
LL10	OS-113285	1290 +/- 25	607	02aN	Twig; coniferous leaf	665-770	656-712	676
LL11	OS-113286	1560 +/- 20	666-667	02aN	Coniferous/deciduous leaf	426-549	437-555	514
LL12	OS-113287	11800 +/- 45	--	--	C5 standard (dead wood)			--
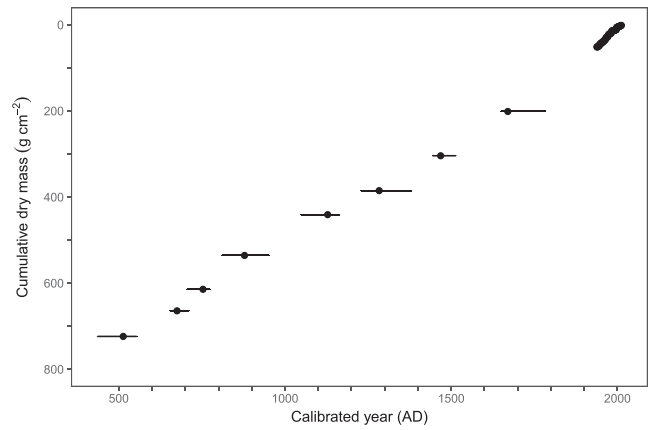
Figure 10. Age–mass model of Core 02aN. Depth is represented on the y-axis by cumulative dry mass down the core. Calibrated ages for eight radiocarbon samples are shown, with the median indicated by a point, and approximate 95% highest posterior density (hpd) ranges as error bars. The contemporary period is shown in the upper right corner.

period (0.44 (0.41–0.46) g cm⁻² y⁻¹). Even the late contemporary period MAR (0.59 (0.48–0.70) g cm⁻² y⁻¹),) cannot be said to be different from the MAR of the gap period because of overlapping CI, and is only slightly faster than the MAR of the early period. If the CI of either the post-1978 contemporary period or the early period were collectively 0.02 g cm⁻² y⁻¹ wider, the rates would overlap. In other words, after 1978, the estimated mean MAR has nearly returned to rates before 1700, but cannot be said to be significantly different from the gap.

Comparison of rates between the gap and other periods is problematic because the gap is not dated directly and also because the CI is large. However, these two issues can be addressed. The CI of the gap period is quite large because resampling is from the whole of the modeled posterior density (MPD) within the LL2 sample, which has a bi-modal distribution with peaks at 1651–1688 AD and 1733–1784 AD (Figures S7 and S8). The lower range is more probable, given prior knowledge of an event that occurred at that time, the 1700 AD earthquake. If only the lower interval of the MPD were used and not the higher interval, event bed E9 would be dated to near 1700 AD, the last known earthquake (Mw 9.00) to have occurred in the region. Furthermore, the event beds E7 and E8 land near 1890 AD and 1770 AD respectively (Figure 3), after large fires, and for E7, after and near known large regional flood events. Using this lower portion of the distribution to calculate the MAR of the gap period we find that the mode of the distribution would have an estimated mean range of 0.53–0.62 g cm⁻² y⁻¹ (Figure S8). This is the expected result, because this is closer to the simple ratio calculation between the two periods, forcing LL2 to 1700 AD, in which the MAR is 0.63 g cm⁻² y⁻¹ (not shown), if the background sediment accumulation rate was uniform. The period comparison result would then be that the MAR of the early contemporary period is significantly higher than the gap period, in that the CI of either period do not overlap.

It would seem then that the estimated mean MAR of the early contemporary period is higher than the whole of the early period, as described above. This is true when comparing with an overall, average MAR of the whole early period. However, the CI is narrow and it cannot be ruled out that sediment accumulation rates varied in the past within shorter periods of time, which we were unable to discern due to lack of material to date and the rarity of varves throughout the early period. By comparing estimated mean MAR between regions bound by ¹⁴C dated layers with MC type resampling, it is evident that the MAR

Table VII. Event beds within age ranges of past CSZ earthquakes. Event bed in bold print is closest to the estimated quake age. The LL ^{14}C age is the median (cal y AD) followed by the median-containing 95% hpd range

LL event beds in stratigraphic proximity of CSZ quake	LL ^{14}C age in stratigraphic proximity (cal y AD, range)	[1]Estimated mean turbidite age (AD)	2σ (RMS) range low, high	[2]Estimated mean quake age by land evidence (AD)	2 SD range low, high	Estimated magnitude of quake (M_w)
9	1671 (1650-1687)	1685	1579-1811	1700[3]	--	9.00[f]
10	1469 (1444-1514)	1469	1377-1566	1474	1252-1696	8.70[f]
10,**11**,12	extrapolate	1402	1289-1524	--	--	8.19[p]
13	1129 (1048-1164)	1154	1044-1271	1199	1104-1294	8.87[f]
15,16,**17**	879 (811-895)	884	774-1008	940	--	8.34[p]
17,18,19,20,**21**	676 (655-711)	707	602-831	728	605-852	8.90[f]
21,22,**23**	514 (436-554)	528	404-664	510	--	8.25[p]
22,23	514 (436-554)	397	220-567	376	274-478	8.80[f]

[1]Quake ages are estimated by mean turbidite ages and mean marsh calibrated ages of coastal subsidence. Root mean square error (RMS) and standard deviations (SD) are listed for the ranges of the turbidite and land ages, respectively. With each estimated magnitude (Mw) is a symbol indicating rupture extent, where f = full rupture of CSZ and p = partial rupture of CSZ.

[2]Dashes in land evidence dates and ranges indicate only one or no recorded event, or in the case of 1700 AD, other definitive evidence. Data for all but left two columns are taken from Goldfinger et al., 2012 (Appendix 01), which compile references within. CSZ = Cascadia subduction zone.

[3]Leonard et al., 2010; Nelson et al., 2006

during the early contemporary period was still higher than all MAR, except between 879 and 676 AD, which largely follows event bed E21 (Table V). However, when event beds are removed (EFD), the estimated mean MAR and CI of 879–676 AD are nearly identical to the MAR and CI of the early contemporary period and similar to that of the gap period.

The increased MARs in the early contemporary period and the gap period can be interpreted that during periods when multiple regolith-destabilizing forcings, such as harvest-floods or fires-floods-earthquakes-land clearance are simultaneously acting on the landscape, the threshold for mobilization and delivery of sediment is lowered. Similarly, the elevated MAR in the period following the large E21 event bed indicates that the regolith had been destabilized by the event, sediment supply was therefore high, and subsequent floods mobilized sediment to the fluvial system and the lake.

Loon Lake's MAR and SAR are much higher than those of most other lakes studied in Oregon, regardless of the time period considered in the stratigraphic column. Compare LL's overall contemporary and early periods' MARs of 0.69, 0.44 g cm^{-2} y^{-1} and SAR 0.89, 0.40 cm y^{-1}, respectively (rates abbreviated here from Table V for ease of comparison), with others measured in Oregon for various time periods. In the OCR, Lost Lake's SAR was ~0.1 cm y^{-1} in the last ~1000 y (Long et al., 2007) and Little Lake's MAR was ~0.14 cm y^{-1} in the last ~1100 y (Long et al., 1998). Adjacent Triangle Lake increased from 0.09 cm y^{-1} (6.0–3.5 k y BP) to 0.17 cm y^{-1} (3.5 k y BP to 1900 AD) to 0.21 cm y^{-1} in the last century (Kusler, 2012). Researchers at Triangle Lake attributed the increase in SAR and MAR to anthropogenic activities in the 20th century. However, two researched lakes had much higher rates. Researchers at Upper Squaw Lake in southern Oregon reported an increase in SAR to ~4 cm y^{-1} from a background of 0.3 cm y^{-1}, attributed to land use (Colombaroli and Gavin, 2010). Dorena Lake, a reservoir in the Cascade Range, was found to have an average rate of 0.55–1.24 cm y^{-1}, with the peak in 1954–1964 AD of 2.1 and 2.7 cm y^{-1} for two cores (Ambers, 2001). Both of these lakes had been highly impacted by land use, and were within different lithologic units. Compared with the other lakes in the OCR or on the coast, LL has both high rates of land use, as well as high elevation relief (Figure 2), which partly explain the difference. A further look at catchment to lake area ratio, precipitation, intensity and magnitude of timber harvest, and other factors would elucidate the differences in accumulation rates.

Hydrologic event correlation

A few studies have demonstrated a correlation between the magnitude of event precipitation (or discharge) and bed thickness (Page et al., 1994, 2010; Brown et al., 2000; Schiefer et al., 2011). For example, at Lake Tutira, New Zealand, which has a daily precipitation record from 1894 to 1988, thicknesses of storm layers were scaled to threshold precipitation amounts, and human impacts on the landscape were shown to lower the threshold of landsliding. Instrumentation does not exist within the LL catchment as in Lake Tutira and a few other sites (Schiefer et al., 2011). However, there is a strong correlation between Elkton Q and layer mass on a log–log scale ($r_s = 0.62$, $p < 0.0001$). The six event beds in the contemporary period (highest mass layers) are correlated with some of the highest peak flows at Elkton gage (Figure 11). However, it is evident in the varved region at the top of the sedimentary column, not all layer masses scale with flood magnitude, as recorded by the Elkton record. For example, the 1965 WY peak Q on the Umpqua at Elkton was the largest on record at that station. The LL layer mass for that year is only 2.8 g cm^{-2}, third from highest in the contemporary sediment record.

Sediment exhaustion and storage within the system is one explanation of why the layer mass does not scale with thickness. Thicker winter layers from 1943 to 1978 indicate that this was a stormy period, reflecting the cool-phase of the PDO, which is reflected in the increase in average annual precipitation and discharge (cf. Wheatcroft et al., 2013). So, perhaps at one time the 1965 event would have been a very large delivery of sediment to the lake, had been lessened because of a few large storms and many moderate storms prior to this event, removing sediment from storage in the fluvial system. The thick deposit in 1997 (E1) may be an example of the corollary, where the PDO had entered a warm-dry phase and less sediment had been transported to the lake in previous years, and an event of lower magnitude than the WY 1965 storm (by the Elkton record) resulted in a much larger deposit because the fluvial system was less supply-limited. There are examples in other research where the magnitude of the event does not produce the expected resulting sediment. At Lake Tutira, Cyclone Bola (1988) with a record 753 mm rainfall produced only 70% of the sediment of a 692-mm precipitation storm (1938) (Page et al., 1994). Outside of lake settings, in Redwood Creek, northern California,
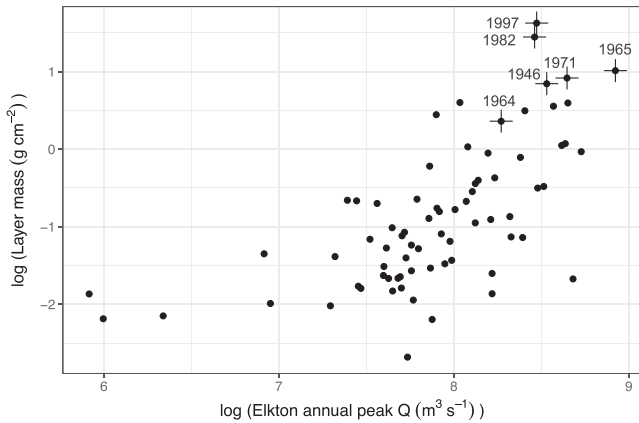
Figure 11. Layer mass and annual peak discharge at Elkton. The relationship is shown by a scatterplot (log–log) of layer mass in the varved contemporary period and annual peak discharge (Q) at the Umpqua R. at Elkton for the water years WY 1939–2012. Event beds E1–6, with the most mass in the contemporary period, are indicated by stars labeled by WY.

two similar storms in that catchment (1955, 1964) produced much different amounts of sediment, the later one producing much more (Kelsey, 1980). In New Zealand, soil was still recovering from the 1938 storm, so 1988 produced less. In California, the first storm may have primed the landscape for the second. In both situations, the threshold of failure had apparently been lowered by land use.

Role of forcings

Most (~84%) of the sedimentary column in LL was formed by background sedimentation, which is largely mass influx from the catchment during annual low- to moderate-discharges. Event beds contribute to 16% of the mass of the core, but within effectively instantaneous time periods. Of the 23 event

beds, it is likely that 20 were deposited by high discharge fluvial inflows that became hyperpycnal flows in the lake. These comprise ~10% of the core by mass, but were deposited in a small fraction of the time represented by the core (e.g., assuming 1 week to form each deposit, then 20 deposits = 0.38 y out of 1500 y or 0.026% of the time). This simple (and conservative) calculation highlights the significant impact of extreme storms in the history of LL.

To further evaluate the significance of event beds, a flood frequency-type analysis was completed for core 02aN. The early part of the core, well before large-scale timber harvesting, was divided into twenty-nine 50-y-long bins (representing calibrated years AD 464–1912). All light layers and thick graded layers were identified within each bin. Two bins did not have visually identifiable light layers, containing only mottled beds and indistinct layers, so these were dropped from the analysis (USGS, 1982). Within each of the remaining 27 bins, the layer with the greatest mass was labeled as the maximum (equivalent to the peak discharge for flood analysis) and a flood frequency analysis was performed (Colombaroli and Gavin, 2010). This analysis yielded return intervals for each of the thickest layers, and enabled a calculation of layer mass at the 2-, 5-, 10-, 25-, 50-, 100-, and 200-y return intervals. A line fitted to the magnitude of the mass of these return intervals describes the relationship based on pre-1912 sedimentary deposits. Assuming stationarity in the erosional and depositional system, the contemporary period can be interpreted within this historical context (Figure 12).

For example, using the fitted line, which approximates a Log Pearson Type III distribution, the thickest layers from the two most recent 50-y bins were interpolated for their return intervals, as were the other four events in the contemporary period (Figure 12). Because the whole-core time period was broken into 50-y bins, return periods were multiplied by 50. Event bed E21 was excluded from the entire analysis because it has very different sedimentary characteristics, implying a different transport mechanism. The results of the 'flood frequency' analysis show all six event beds in the years 1939-2012 AD apparently have return intervals from 90 to 300 y, and the two largest beds in the latest two 50-y bins, 2.3 g cm^{-2} and 5.1 g cm^{-2}
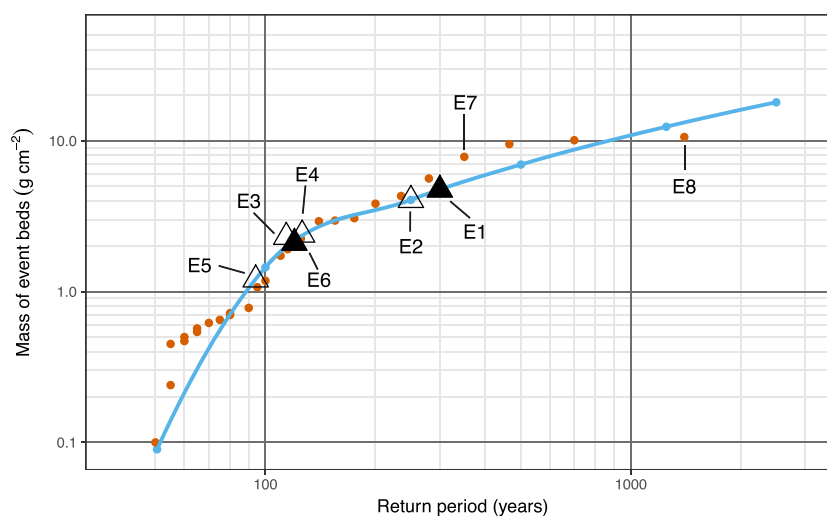

Figure 12. Flood frequency-type analysis for mass of event beds in Core 02aN. From the data analysis, the line (blue) with points on the line approximate a Log Pearson Type III distribution. Floating points (red) represent the largest event beds by dry mass in 50-y bins of the core back to ~460 cal year AD. The last 100 y are not part of the analysis, but are instead represented by two filled triangles at interpolated return periods on the distribution, WY 1946 and 1997. The open triangles show the mass of the other event beds in the last 100 y, and their interpolated return periods on the distribution. E7 and E8 were part of the analysis, and are indicated by name. The analysis excluded E21 because this event has very different sedimentary characteristics, implying a different mechanism. A loess smoothing method was applied to the blue distribution line with a span of 0.7 to control the amount of smoothing. [Colour figure can be viewed at wileyonlinelibrary.com]

during 1946 and 1997, respectively, had return periods of 115 and 300 y. Furthermore, during the last 74 y (contemporary period), there have been more events per length of the core (Table IV). There has been a higher incidence of events in the contemporary period and the sediment fluxes associated with these events as a whole has been unusually large. For example, the percent increase of early contemporary period MAR and overall contemporary MAR above the overall early period MAR is 89% and 59%, respectively (Table V), although this is far below the 13-fold increase calculated at Upper Squaw Lake attributed to timber harvest (Colombaroli and Gavin, 2010). Another way of illustrating the mass contribution of the event beds in the LL contemporary period is by the ratio of all-depths MAR to the background (EFD) MAR. The late contemporary MAR is 2.1 times its EFD MAR, compared with 1.5, 1.6, and 1.2 of early contemporary, overall contemporary, and overall early period EFD MARs, respectively.

During the contemporary period, two forcings – timber harvest and floods – acted synergistically upon the catchment to produce elevated sedimentation in the lake. During the time of the cool-phase of the PDO timber harvest was at its peak in the catchment. Not only were there four graded beds indicating large storms with sustained sediment input during this period, most of the other years had thick winter layers, indicating moderate size storms, so the MAR was elevated. As the PDO phase switched to warm and dry, average annual sediment accumulation in the lake decreased immediately, even as timber harvest continued. However, the two thick event beds in 1997 and 1982 in response to large storms contributed a large portion of the sediment to the lake (Ambers, 2001). Indeed, annualized sedimentation as a result of events was not appreciably different between the early- and late-contemporary periods (0.23 and 0.27 g cm^{-2}, respectively). These results indicate that the catchment had stored sediment in the fluvial system and/or hillslopes from previous perturbation (Reid and Page, 2002; May and Gresswell, 2004), and it was then delivered at an elevated discharge, but by storms with a lower recurrence interval than would have been necessary without a prior sediment-producing perturbation.

A second example of forces acting together to deliver sediment occurred before large-scale anthropogenic impact, during the gap period. During the mid-1700s and mid-1800s large fires and storms occurred in the catchment. Essentially, denudation of the landscape by fire may have acted in the same role that timber harvest played later, which is to produce sediment that the moderate and extreme storms will bring to the lake. In a study of post-fire sediment fluxes in a coastal central California catchment, Warrick et al. (2012) found that post-fire annual sediment yield was an order-of-magnitude greater in wet winters than those winters with minimal precipitation. Earthquakes and land clearance may have also primed the landscape during this period as well. At 1700 AD, the CSZ Mw 9.0 earthquake, which although it does not appear to have left a very large event bed (most likely E9), may have primed the landscape for subsequent landsliding and increased hillslope erosion. Additionally, this gap period includes early logging which would have been impactful on soil and streambeds. This time also included the beginning of land clearance in Ash Valley above the lake, which resulted in loss of streambank vegetative root strength. It is about this time that the two unusual deposits E7 and E8 were added to the lake, and have return periods greater than 300 y (Figure 12).

While earthquakes themselves can contribute sediment directly to LL by co-seismic failures (e.g. E21) or post-seismic failures, most earthquake-driven sedimentation must be through the fluvial system. At Lake Paringa in New Zealand, it was found that average sedimentation rate by aseismic deposition

was 0.21 ± 0.05 g cm^{-2} y^{-1}, and post-seismic was 0.60 ± 0.21 g cm^{-2} y^{-1}, and the least mass of the three mechanisms by co-seismic deposition (Howarth et al., 2012). At LL, sediment produced and delivered strictly by earthquakes could not be separated from that produced and delivered from other perturbations, although many event beds are coeval in time with estimated ages of earthquakes. Apparently, however, besides during peak timber harvest, MAR was highest in the entire sedimentary column following two earthquakes with the largest estimations of magnitude in the lifetime of this core – 1700 and ~700 AD (Tables IV and VI).

Throughout time in this core, regardless of which event occurred in the catchment and the variability of the measured parameters of each event, the background sedimentation had little variance (Figure 7), but the sediment flux in the contemporary period increased. Earthquake and fires have acted through most of the history of the core, providing sediment to the lake by large storms, but also by extra sediment delivered by normal winter precipitation. Timber harvest has acted in a short time, but similar to earthquake and fire, has increased supply of sediment to the fluvial system. Nearly all sediment has been driven to the lake by floods of varying magnitude.

All of these forcings act on the landscape, and the landscape recovers with time. Burned over areas regenerate vegetation, harvested areas regrow, evacuated hollows from landslides rebuild soil and regenerate vegetation. However, as long as timber harvest and associated roads exist, they are acting as the sediment-driving force that has replaced the catchment's next highest recurrence interval disturbance – pre-suppression forest fire (Kennedy and Spies, 2004).

Conclusions

The fidelity of the sedimentary record is high in the eutrophic contemporary period allowing for annual analysis of sedimentary dynamics. During the early contemporary period of this core, 1939–1978, which is the period of peak timber harvest in the catchment and the cool-wet phase of the PDO, the mass accumulation rate (MAR) was significantly higher than in 1979–2012. Even when event deposit mass is removed (event-free depth), the difference in the rates between the two periods is still significant. The two forcings at work during this period – timber harvest activities and floods – cannot be disentangled, and the possible moderating influence of better forest harvest practices could not be confidently identified with our techniques.

The first 1100 y of the sedimentary column (515–1671 AD) has a lower estimated mean MAR than the 75 y of the contemporary period and the 270-y-long period in between (1671–1939 AD). It appears that the estimated MAR during the early contemporary period is higher than most of the rest of the core and that timber harvesting and associated road building may be associated with a lowering of the threshold by which extreme hydrologic events mobilize and deliver sediment to the lake.

The consequence of multiple forcings acting together, such as harvest activities and floods, is to increase MAR, as was also the case during the gap period (between 1671 and 1939 AD), when large fires, extreme floods, and the possible destabilization of hillslopes occurred following the 1700 AD CSZ Mw 9.0 earthquake. Earthquakes are probably recorded in the sediment by co-seismic landscape destabilization and post-seismic sediment delivery to the lake by moderate and high-magnitude flood events in the form of hyperpycnal flows, and likely on at least one occasion by a debris flow delivered directly to the lake.

References

Allen PA. 2008. From landscapes into geological history. *Nature* **451**: 17–20.

Ambers R. 2001. Using the sediment record in a western Oregon flood-control reservoir to assess the influence of storm history and logging on sediment yield. *Journal of Hydrology* **244**: 181–200.

Anderson CJ, Lockaby BG. 2011. Research gaps related to forest management and stream sediment in the United States. *Environmental Management* **47**: 303–313.

Aust WM, Blinn CR. 2004. Forestry best management practices for timber harvesting and site preparation in the eastern United States: an overview of water quality and productivity research during the past 20 years (1982–2002). *Water, Air, and Soil Pollution* **4**: 5–36.

Baldwin EM. 1974. Eocene stratigraphy of southwestern Oregon. Oregon Department of Geology and Mineral Industries Bulletin 83.

Beschta RL. 1978. Long-term patterns of sediment production following road construction and logging in the Oregon Coast Range. *Water Resources Research* **14**: 1011–1016.

Beschta RL, Jackson WL. 2008. Forest practices and sediment production in the Alsea Watershed Study. In *Hydrological and Biological Responses to Forest Practices: The Alsea Watershed Study*, Stednick J (ed). Springer Science + Business Media LLC: New York, NY; 55–66.

Besonen MR, Patridge W, Bradley RS, Francus P, Stoner JS, Abbott MB. 2008. A record of climate over the last millennium based on varved lake sediments from the Canadian High Arctic. *The Holocene* **18**: 169–180.

Björck S, Wohlfarth B. 2001. [14]C chronostratigraphic techniques in paleolimnology. In *Tracking Environmental Change Using Lake Sediments. Volume 1: Basin Analysis, Coring, and Chronological Techniques*, Last WM, Smol JP (eds). Kluwer Academic Publishers: Dordrecht; 1–41.

Blaauw M. 2010. Methods and code for "classical" age-modelling of radiocarbon sequences. *Quaternary Geochronology* **5**: 512–518.

Bronk Ramsey C. 2008. Deposition models for chronological records. *Quaternary Science Reviews* **27**: 42–60.

Bronk Ramsey C. 2009a. Bayesian analysis of radiocarbon dates. *Radiocarbon* **51**: 337–360.

Bronk Ramsey C. 2009b. Dealing with outliers and offsets in radiocarbon dating. *Radiocarbon* **51**: 1023–1045.

Bronk Ramsey C, Staff RA, Bryant CL, Brock F, Kitagawa H, van der Plicht J, Schlolaut G et al. 2012. A complete terrestrial radiocarbon record for 11.2 to 52.8 kyr B.P. *Science* **338**: 370–374.

Brown S, Bierman PR, Lini A, Davis PT, Southon J. 2002. Reconstructing lake and drainage basin history using terrestrial sediment layers: analysis of cores from a post-glacial lake in NE, USA. *Journal of Paleolimnology* **28**: 219–236.

Brown S, Bierman PR, Lini A, Southon J. 2000. 10000 yr record of extreme hydrologic events. *Geology* **28**: 335–338.

Cohen AS. 2003. *Paleolimnology: The History and Evolution of Lake Systems.* Oxford University Press: New York.

Cohen WB, Spies TA, Alig RJ, Oetter DR, Maiersperger TK, Fiorella M. 2002. Characterizing 23 years (1972-95) of stand replacement disturbance in western Oregon forests with Landsat imagery. *Ecosystems* **5**: 122–137.

Colombaroli D, Gavin DG. 2010. Highly episodic fire and erosion regime over the past 2000 y in the Siskiyou Mountains, Oregon. *Proceedings of the National Academy of Sciences of the United States of America* **107**: 18909–18914.

Cristan R, Aust WM, Bolding MC, Barrett SM, Munsell JF, Schilling E. 2016. Effectiveness of forestry best management practices in the United States: literature review. *Forest Ecology and Management* **360**: 133–151.

Crozier MJ. 1986. *Landslides: Causes, Consequences, and Environment.* Kent, UK: Croom Helm Ltd.

Curtiss DA, Collins CA, Oster EA. 1984. Water-Resources of Western Douglas Co., Oregon. US Geological Survey Water-Resources Investigations, Report 83-4017.

Dadey KA, Janecek T, Klaus A. 1992. Dry-bulk density: its use and determination. In *Proceedings of the Ocean Drilling Program, Scientific Results*, Taylor B, Fujioka K et al. (eds). National Science Foundation, & Joint Oceanographic Institutions Incorporated: College Station, TX, USA; Vol. **126**; 551–554.

Dearing JA. 1991. Lake sediment records of erosional processes. *Hydrobiologia* **214**: 99–106.

Dean WE, Bradbury JP. 1993. Characteristics of sediments from selected lakes of Oregon and Washington and their potential for obtaining high-resolution paleoclimate records. US Geological Survey Open-File Report 93-212.

Dietrich WE, Dunne T. 1978. Sediment budget for a small catchment in mountainous terrain. *Zeitschrift für Geomorphologie, Supplementband* **29**: 191–206.

Edmondson WT. 1991. Sedimentary record of changes in the condition of Lake Washington. *Limnology and Oceanography* **36**: 1031–1044.

ESRI, Environmental Systems Research Institute. 1998. *ARCMAP.* Environmental Systems Research Institute Inc.: Redlands, California.

Franklin JF, Dyrness CT. 1988. *Natural Vegetation of Oregon and Washington.* OSU Press, Oregon State University: Corvallis, Oregon.

Goldfinger C, Nelson CH, Morey AE, Johnson JE, Patton JR, Karabanov E, Gutiérrez-Pastor J, *et al.* 2012. Turbidite Event History – Methods and Implications for Holocene Paleoseismicity of the Cascadia Subduction Zone. US Geological Survey Professional Paper 1661-F.

Gray AB, Pasternack GB, Watson EB. 2010. Hydrogen peroxide treatment effects on the particle size distribution of alluvial and marsh sediments. *The Holocene* **20**: 293–301.

Hairston-Strang AB, Adams PW, Ice GG. 2008. The Oregon Forest Practices Act and Forest Research. In *Hydrological and Biological Responses to Forest Practices*, Stednick JD (ed). Springer: Berlin; 95–113.

Hatten JA, Goni MA, Wheatcroft RA. 2012. Chemical characteristics of particulate organic matter from a small, mountainous river system in the Oregon Coast Range, USA. *Biogeochemistry* **107**: 43–66.

Hatten JA, Segura C, Bladon K, Hale VC, Ice G, Stednick J. 2018. Effects of contemporary forest harvesting on suspended sediment in the Oregon Coast Range: Alsea Watershed Study Revisited. *Forest Ecology and Management* **408**: 238–248.

Hedges JI, Stern JH. 1984. Carbon and nitrogen determinations of carbonate containing solids. *Limnology and Oceanography* **49**: 657–663.

Heimsath AM, Dietrich WE, Nishiizumi K, Finkel RC. 2001. Stochastic processes of soil production and transport: Erosion rates, topographic variation and cosmogenic nuclides in the Oregon Coast Range. *Earth Surface Processes and Landforms* **26**: 531–552.

Ho I, Ching-Yan L. 1987. Microbial and chemical properties of log ponds along the Oregon coast. US Department of Agriculture, Forest Service, Pacific Northwest Research Station. Research Note PNW-RN-467.

Hofmann MH, Hendrix MS. 2010. Depositional processes and the inferred history of ice-margin retreat associated with the deglaciation

of the Cordilleran Ice Sheet: The sedimentary record from Flathead Lake, northwest Montana, USA. *Sedimentary Geology* **223**: 61–74.

Hovius N, Meunier P, Ching-Weei L, Hongey C, Yue-Gau C, Dadson S, Ming-Jame H, Lines M. 2011. Prolonged seismically induced erosion and the mass balance of a large earthquake. *Earth and Planetary Science Letters* **304**: 347–355.

Howarth JD, Fitzsimons SJ, Jacobsen GE, Vandergoes MJ, Norris RJ. 2013. Identifying a reliable target fraction for radiocarbon dating sedimentary records from lakes. *Quaternary Geochronology* **17**: 68–80.

Howarth JD, Fitzsimons SJ, Norris RJ, Jacobsen GE. 2012. Lake sediments record cycles of sediment flux driven by large earthquakes on the Alpine fault, New Zealand. *Geology* **40**: 1091–1094.

Ice G. 2004. History of innovative best management practice development and its role in addressing water quality limited waterbodies. *Journal of Environmental Engineering, ASCE* **130**: 684–689.

Jackson M, Roering JJ. 2009. Post-fire geomorphic response in steep, forested landscapes: Oregon Coast Range, USA. *Quaternary Science Reviews* **28**: 1131–1146.

Jones JA, Grant G. 1996. Peak flow responses to clear-cutting and roads in small and large basins, western Cascades, Oregon. *Water Resources Research* **32**: 959–974.

Karlin RE, Abella SE. 1992. Paleoearthquakes in the Puget Sound region recorded in sediments from Lake Washington, U.S.A. *Science* **258**: 1617–1620.

Karlin RE, Holmes M, Abella SEB, Sylwester R. 2004. Holocene landslides and a 3500-year record of PNW earthquakes from sediments in Lake Washington. *Geological Society of America Bulletin* **116**: 94–108.

Kennedy RSH, Spies TA. 2004. Forest cover changes in the Oregon Coast Range from 1939 to 1993. *Forest Ecology and Management* **200**: 120–147.

Kelsey HM. 1980. A sediment budget and an analysis of geomorphic process in the Van-Duzen River basin, north coastal California, 1941-1975 – summary. *Geological Society of America Bulletin* **91**: 190–195.

Kennedy RE, Yang ZQ, Cohen WB, Pfaff E, Braaten J, Nelson P. 2012. Spatial and temporal patterns of forest disturbance and regrowth within the area of the Northwest Forest Plan. *Remote Sensing of Environment* **122**: 117–133.

Keppeler ET. 2012. Sediment production in a coastal watershed: legacy, land use, recovery, and rehabilitation. In *Proceedings of coast redwood forests in a changing California: A symposium for scientists and managers*, Standiford RB, Weller TJ, Piirto DD, Stuart JD (eds), Gen. Tech. Rep. PSW-GTR-238. Pacific Southwest Research Station, Forest Service, US Department of Agriculture: Albany, CA; 69–77.

Kusler J. 2012. A 7500-year paleolimnological record of environmental change and salmon abundance in the Oregon Coast Range. MS thesis. Eugene, University of Oregon.

Leonard LJ, Currie CA, Mazzotti S, Hyndman RD. 2010. Rupture area and displacement of past Cascadia great earthquakes from coastal coseismic subsidence. *Geological Society of America Bulletin* **122**: 2079–2096.

Litschert SE, MacDonald LH. 2009. Frequency and characteristics of sediment de- livery pathways from forest harvest units to streams. *Forest Ecology and Management* **259**: 143–150.

Long CJ, Whitlock C, Bartlein PJ. 2007. Holocene vegetation and fire history of the Coast Range, western Oregon, USA. *The Holocene* **17**: 917–926.

Long CJ, Whitlock C, Bartlein PJ, Millspaugh SH. 1998. A 9000-year fire history from the Oregon Coast Range, based on a high-resolution charcoal study. *Canadian Journal of Forest Research* **28**: 774–787.

Mantua NJ, Hare SR, Zhang Y, Wallace JM, Francis RC. 1997. A Pacific interdecadal climate oscillation with impacts on salmon production. *Bulletin of the American Meteorological Society* **78**: 1069–1079.

May CL, Gresswell RE. 2004. Spatial and temporal patterns of debris-flow deposition in the Oregon Coast Range, USA. *Geomorphology* **57**: 135–149.

Minckley T, Whitlock C. 2000. Spatial variation of modern pollen in Oregon and southern Washington, USA. *Review of Palaeobotany and Palynology* **112**: 97–123.

Moreno A, Valero-Garcés BL, González-Sampériz P, Rico M. 2008. Flood response to rainfall variability during the last 2000 years inferred from the Taravilla Lake record (Central Iberian Range, Spain). *Journal of Paleolimnology* **40**: 943–961.

Morey AE, Goldfinger C, Briles CE, Gavin DG, Colombaroli D, Kusler JE. 2013. Are great Cascadia earthquakes recorded in the sedimentary records from small forearc lakes? *Natural Hazards and Earth System Sciences* **13**: 2441–2463.

Mulder T, Alexander J. 2001. The physical character of subaqueous sedimentary density flows and their deposits. *Sedimentology* **48**: 269–299.

Nelson AR, Kelsey HM, Witter RC. 2006. Great earthquakes of variable magnitude at the Cascadia subduction zone. *Quaternary Research* **65**: 354–365.

Nesje A. 1992. A piston corer for lacustrine and marine sediments. *Arctic and Alpine Research* **24**: 257–259.

Oregon. 2001. Oregon Forest Practices Act. State of Oregon. Accessed from http://www.oregon.gov/ODF/Working/Pages/FPA.aspx

Oregon DEQ. 1992. Laboratory Analytical Storage and Retrieval (LASAR), Station 13813. Oregon Department of Environmental Quality. Accessed from http://deq12.deq.state.or.us/lasar2/

Orpin AR, Carter L, Page MJ, Cochran UA, Trustrum NA, Gomez B, Palmer AS et al. 2010. Holocene sedimentary record from LakeTutira: A template for upland watershed erosion proximal to the Waipaoa Sedimentary System, northeastern New Zealand. *Marine Geology* **270**: 11–29.

Owens P, Slaymaker O. 1993. Lacustrine sediment budgets in the coast mountains of British Columbia, Canada. In *Geomorphology and Sedimentology of Lakes and Reservoirs*, McManus J, Duck RW (eds). John Wiley & Sons: Chichester; 105–123.

Page MJ, Trustrum NA, DeRose RC. 1994. A high resolution record of storm induced erosion from lake sediments, New Zealand. *Journal of Paleolimnology* **11**: 333–348.

Page MJ, Trustrum NA. 2010. Storm frequency and magnititude in response to Holocene climate variability, Lake Tutira, North-Eastern New Zealand. *Marine Geology* **270**: 30–44.

PRISM Climate Group. 2004. PRISM Gridded Climate Data. Oregon State University, Corvallis, OR. Accessed from http://prism.oregonstate.edu

R Development Core Team. 2016. *R: A Language and Environment for Statistical Computing*. R Foundation for Statistical Computing: Vienna.

Ralph FM, Dettinger MD. 2012. Historical and national perspectives on extreme west coast precipitation associated with atmospheric rivers during December 2010. *Bulletin of the American Meteorological Society* **93**: 783–790.

Ramsey F, Schafer D. 2013. *The Statistical Sleuth*, 3rd edn. Brooks/Cole: Boston, MA, USA.

Reid LM, Page MJ. 2002. Magnitude and frequency of landsliding in a large New Zealand catchment. *Geomorphology* **49**: 71–88.

Reimer PJ, Bard E, Bayliss A, Beck JW, Blackwell PG, Bronk Ramsey C, Grootes PM et al. 2013. IntCal13 and Marine13 radiocarbon age calibration curves 0-50,000 years cal BP. *Radiocarbon* **55**: 1869–1887.

Reneau SL, Dietrich WE. 1990. Depositional history of hollows on steep hillslopes, coastal Oregon and Washington. *National Geographic Research* **6**: 220–230.

Richardson KND. 2017. Role of Extreme Events on Sedimentation in Loon Lake, Oregon Coast Range, USA. MS thesis. Corvallis, Oregon State University.

Rinella JF. 1979. Lakes of Oregon. Volume 6: Douglas County. US Geological Survey Open-File Report.

Roering JJ, Gerber M. 2005. Fire and the evolution of steep, soil-mantled landscapes. *Geology* **33**: 349–352.

Roering JJ, Kirchner JW, Dietrich WE. 2005. Characterizing structural and lithologic controls on deep-seated landsliding: Implications for topographic relief and landscape evolution in the Oregon Coast Range, USA. *Geological Society of America Bulletin* **117**: 654–668.

Schiefer E, Gilbert R, Hassan MA. 2011. A lake sediment-based proxy of floods in the Rocky Mountain Front Ranges, Canada. *Journal of Paleolimnology* **45**: 137–149.

Schuytema GS, Shankland RD. 1976. Effects of Log Handling and Storage on Water Quality. US Environmental Protection Agency. Environmental Protection Technology Series EPA-600/2-76-262. Cincinnati, Ohio.

Sperazza M, Moore JN, Hendrix MS. 2004. High-resolution particle size analysis of naturally occurring very fine-grained sediment through laser diffractometry. *Journal of Sedimentary Research* **74**: 736–743.

Swanson FJ. 1981. Fire and geomorphic processes. In Proceedings, Fire Regimes and Ecosystems Conference. US Department of Agriculture, Forest Service, General Technical Report WO-26, Honolulu, Hawaii; 401–420.

Swanson FJ, Jones JA. 2002. Geomorphology and hydrology of the H.J. Andrews Experimental Forest, Blue River, Oregon. In *Field Guide to Geologic Processes in Cascadia*, Moore GW (ed). Oregon Department of Geology and Mineral Industries: Corvallis, OR; 289–314.

Telford RJ, Heegaard E, Birks HJB. 2004. The intercept is a poor estimate of a calibrated radiocarbon age. *The Holocene* **14**: 296–298.

USDI. 2005. Mill Creek-Lower Umpqua River Watershed Analysis. US Department of Interior, Coos Bay District, Umpqua Resource Area – Bureau of Land Management.

USGS. 1982. United States Geological Survey. Guidelines for Determining Flood Frequency Analysis. Bulletin #17B of the Hydrology Subcommittee.

USGS. 2012. United States Geological Survey. Shakemap scenario. Accessed from https://earthquake.usgs.gov/scenarios/eventpage/gllegacycasc9p0expanded_se

Warrick JA, Hatten JA, Pasternack GB, Gray AB, Goni MA, Wheatcroft RA. 2012. The effects of wildfire on the sediment yield of a coastal California watershed. *Geological Society of America Bulletin* **124**: 1130–1146.

Wetzel RG. 2001. *Limnology: Lake and River Ecosystems*, 3rd edn. San Diego: Academic Press.

Wheatcroft RA. 1990. Preservation potential of sedimentary event layers. *Geology* **18**: 843–845.

Wheatcroft RA, Goni MA, Richardson KN, Borgeld JC. 2013. Natural and human impacts on centennial sediment accumulation patterns on the Umpqua River margin, Oregon. *Marine Geology* **339**: 44–56.

Wheatcroft RA, Sommerfield CK. 2005. River sediment flux and shelf sediment accumulation rates on the Pacific Northwest margin. *Continental Shelf Research* **25**: 311–332.

Witter RC, Zhang YL, Wang KL, Goldfinger C, Priest GR, Allan JC. 2012. Coseismic slip on the southern Cascadia megathrust implied by tsunami deposits in an Oregon lake and earthquake-triggered marine turbidites. *Journal of Geophysical Research - Solid Earth* **117**: B10303.

Zolitschka B, Francus P, Ojala AEK, Schimmelmann A. 2015. Varves in lake sediments – a review. *Quaternary Science Reviews* **117**: 1–41.

Zuur AF, leno EN, Walker N, Saveliev AA, Smith GM. 2009. Mixed Effects Models and Extensions in Ecology with R.

Supporting Information

Additional Supporting Information may be found online in the supporting information tab for this article.

Table S1. List of catchment events since 1700 AD. These may have contributed sediment to Loon Lake, or contribute to an understanding of sedimentation at Loon Lake. [1]Leonard *et al.*, 2010; [2]ODF, 2011; [3]Phillips J, 2015; [4]Biosystems, 2003; [5]Douglas Co., 2009; [6]Sims, 1998; [7]USGS, 2013; [8]Snyder et al., 2006; [9]USDI, 2005; [10]USACE, 2000; [11]Jones and Stearns, 1928

Figure S1. Total and partial percent of catchment harvested from 1943 to 2014. Black line with filled circles is satellite-derived *total* percent of catchment from 1985 to 2012. Grey line with square hollow points is *partial* percent of the total catchment which was harvested each y from 1943 to 2014 only by the largest private landowner (70% ownership of the catchment).

Figure S2. Whole-core grain size and geochemistry, photo, and stratigraphic units. Parameters included are dry bulk density, C:N (atomic), % total nitrogen, % total carbon, % clay, and median grain size (D_{50}). The sedimentary column is split into two halves: 0-340 cm and 340-694 cm in MSCL depth scale.

Below the six parameters is the length scale in cm according to the MSCL depth, which is correlated with the photograph of the core. The stratigraphic unit cartoon (legend below) is correlated with the x-radiograph. D_{50} of event bed E21 spikes to 231 μm, and is shown rising above all other parameter plots. Buttons visible in the core photograph are misplaced below the top section at 143 cm, therefore use the MSCL depth scale.

Figure S3. To characterize the %TC, %TN, and C:N of the thin dark laminae and thicker light layers at the top 10 cm of a reconnaissance core, 8 structural samples of the two layer types were collected and analyzed as above (n=16). Geochemistry results of structural sampling are represented by boxplots of % total carbon, % total nitrogen and C/N.

Figure S4. Bivariate plots of water discharge at Elkton and Mill Cr. Discharge is from 1908 to 1917 on Mill Creek and on Umpqua River near Elkton. Mill Creek gaging station (USGS #14323000) is downstream of Loon Lake and was operational for seven complete water years during this time. Elkton gaging station (USGS #14321000) is ~20 km east of Loon Lake on the Umpqua R. (Figure 1). a) Monthly peak discharge b) Annual peak discharge.

Figure S5. Annual peak discharge on the Umpqua R. at Elkton. For this station (USGS #14321000), this is the period of record, WY 1906-2013. Cool-wet phase of the PDO is shaded gray.

Figure S6. Age-depth model output from Oxcal. 68%, 95%, and 98% interpolated ranges are drawn between the marginal posterior densities. At each calibrated sample, the light gray distribution is the unmodeled likelihood probability distribution, and the darkened distribution is the posterior probability distribution. Oxcal v4.2.4 (Bronk Ramsey, 2013), based on the IntCal atmospheric curve (Reimer *et al.*, 2013).

Figure S7. OxCal output of ^{14}C sample LL2 probability distributions. Blue line is the calibration curve, red distribution is the sample radiocarbon determination, light gray peaks are the likelihood probability distributions (the intersection of the unmodeled determination with the calibration curve), and dark gray peaks are the marginal posterior densities (the intersection of the OxCal modeled determination with the calibration curve), and brackets mark the 95.4% highest posterior density (hpd) range intervals. The far-right likelihood probability distribution interval (light gray, 1925 AD forward) was eliminated from the Monte Carlo resampling method when calculating accumulation rates. Source is Oxcal (Bronk Ramsey, 2013), based on the IntCal atmospheric curve (Reimer *et al.*, 2013).

Figure S8. Distribution of mass accumulation rates between LL2 and 1939. Method is by Monte Carlo resampling of marginal posterior densities of modeled calibrated dates of ^{14}C sample LL2 and 1939 AD +/- 2y, with replacement, 5000 times. Solid line is the median of the distribution. Dashed line is the mean. The left mode of the distribution is the result of the draws from the left range of the LL2 distribution.

Table S2. Results of tests of difference in MAR in contemporary period. Dry mass accumulation rate (g cm^{-2}y^{-1}) for all depths and event-free depth (EFD) with different regression models are used. Each set includes the estimated mean rate (slope) and difference in slopes, 95% confidence interval (CI), and F-test results for difference in slopes with numbers of degrees of freedom. The estimated mean difference is significant in both cases for our chosen alpha (a=0.05). Models are shown with normal coefficients and standardized coefficients. WY = water year; AM = accumulated mass (g cm^{-2}); Q = discharge (m^3 s^{-1}). Test is a separate lines model of multiple linear regression, where the regression is accomplished by generalized least squares and an AR1 autocorrelation function and a variance structure to account for residual autocorrelation and heterogeneity, respectively.